Geochemical and spectroscopic investigation of apatite in the Siilinjärvi carbonatite complex: Keys to understanding apatite forming processes and assessing potential for rare earth elements

Sophie Decrée [a,*], Mikko Savolainen [b], Julien Mercadier [c], Vinciane Debaille [d], Stefan Höhn [e], Hartwig Frimmel [e], Jean-Marc Baele [f]

[a] Royal Belgian Institute of Natural Sciences-Geological Survey of Belgium, Brussels, Belgium
[b] Yara Suomi Oy, Siilinjärvi, Finland
[c] Université de Lorraine, CNRS, CREGU, GeoRessources, F-54000, Nancy, France
[d] Vinciane Debaille, DGES – Laboratoire G-Time (CP 160/02), Université Libre de Bruxelles (ULB), Brussels, Belgium
[e] Bavarian Georesources Centre, Dept. of Geodynamics and Geomaterials Research, Institute of Geography and Geology, University of Würzburg, Germany
[f] Department of Geology and Applied Geology, University of Mons, Mons, Belgium

ARTICLE INFO

ABSTRACT

The Siilinjärvi phosphate deposit (Finland) is hosted by an Archean carbonatite complex. The main body is composed of glimmerite, carbonatite and combinations thereof. It is surrounded by a well-developed fenitization zone. Almost all the rocks pertaining to the glimmerite-carbonatite series are considered for exploitation of phosphate. New petrological and in-situ geochemical as well as spectroscopic data obtained by cathodoluminescence, Raman and laser-induced breakdown spectroscopy make it possible to constrain the genesis and evolution of apatite through time. Apatite in the glimmerite-carbonatite series formed by igneous processes. An increase in rare earth elements (REE) content during apatite deposition can be explained by re-equilibration of early apatite (via sub-solidus diffusion at the magmatic stage) with a fresh carbonatitic magma enriched in these elements. This late carbonatite emplacement has been known as a major contributor to the overall P and REE endowment of the system and is likely connected to fenitization and alkali-rich fluids. These fluids - enriched in REE - would have interacted with apatite in the fenite, resulting in an increase in REE content through coupled dissolution–reprecipitation processes. Finally, a marked decrease in LREE is observed in apatite hosted by fenite. It highlights the alteration of apatite by a REE-poor fluid during a late-magmatic/hydrothermal stage. Regarding the potential for REE exploitation, geochemical data combined with an estimation of the reserves indicate a sub-economic potential of REE to be exploited as by-products of phosphate mining. Spectroscopic analyses further provide helpful data for exploration, by determining the P and REE distribution and the enrichment in carbonatite and within apatite.

1. Introduction

Phosphate is one of the main commodities mined from alkaline complexes and carbonatites. It has been exploited - mainly to produce fertilizer - in South Africa, Zimbabwe, Brazil, Finland, and Sri Lanka (Verwoed, 1986; Pell, 1996; Van Straaten, 2002). Beside phosphate, it has been shown that numerous critical raw materials – as defined by the European Commission (EC, 2014) – could be recovered from phosphate deposits of this type, namely the rare earth elements (REE), fluorine (fluorspar), and vanadium (Ihlen et al., 2014; Goodenough et al., 2016; Decrée et al., 2017). For instance, magmatic apatite usually contains more than 0.35% REE (Ihlen et al., 2014), in exceptional cases reaching as much as 21 wt % REE_2O_3 (e.g., Roeder et al., 1987; Hughes et al., 1991; Hoshino et al., 2016). With a theoretical maximal content of 3.73 wt% F in apatite, phosphate rocks can contain up to 3–4% F (Notholt et al., 1979). Phosphate formation and accumulation in these rocks can result from various processes that range from magmatic to hydrothermal (metasomatic) to supergene alteration (e.g., Walter et al., 1995;

Broom-Fendley et al., 2016, 2017; Chakhmouradian et al., 2017; Decrée et al., 2015, 2016, 2020). These processes also affect the content of other elements (such as F and REE) in apatite, leading locally to significant enrichment and economic potential of these resources as by-product of phosphate production (Ihlen et al., 2014; Decrée et al., 2016). The spatial superimposition of these processes can make the understanding of the genesis of a given phosphate deposit, and its enrichment in critical raw materials, fairly complex. The objective of this work is to assess the relative importance of each individual crystallization stage in the various facies of the Neoarchean Siilinjärvi Carbonatite Complex (Finland), through a careful petrographic and geochemical study of apatite.

The Siilinjärvi deposit is related to a carbonatite complex dated at ~2610 Ma (Bayanova, 2006; GTK unpublished report in O'Brien et al., 2015). The complex is of lenticular shape, comprises intermixed carbonatite and glimmerite, and dips steeply into a gneissic basement (O'Brien et al., 2015). Fenite is well developed all around the complex. Almost all the glimmerite-carbonatite rocks constitute phosphate ore, with an apatite content of about ~10 vol%. Apatite-rich carbonatite and glimmerite contain up to 30 vol% apatite, and apatite veins are essentially monomineralic (~80 vol% apatite; O'Brien et al., 2015). The Siilinjärvi mine produces about 11 Mt/yr, with ore reserves of 234 Mt at an average grade of 4 wt% P_2O_5 (data for January 2014; O'Brien et al., 2015). The Siilinjärvi deposit has a potential for recovering REE and F. The REE content in apatite was estimated at 0.3–0.4 wt% REE (based on analyses on mineral separates; Puustinen, 1971; Hornig-Kjarsgaard, 1998), though the REE content in whole rock samples varies significantly (from 0.05 to 0.16 wt%; Hornig-Kjarsgaard, 1998). The fluorine content reported for the apatite typically ranges from 2.3 to 3.5 wt% (based on electron microprobe analyses; Puustinen and Kauppinen, 1989; Al Ani, 2013).

Studies focusing on the mineralogy and chemistry of apatite from Siilinjärvi are scarce. Apart from the analyses referred to above, a microthermometric study by Poutiainen (1995) corroborated a primary igneous origin of the apatite and the involvement of an aqueous fluid during fracturing and recrystallization of this mineral. A few isotopic studies on apatite separates from Siilinjärvi have given more information about the origin of this mineral. Based on Nd, δD and δ13C isotope data, it appears that apatite retained its primary mantle-derived signature and formed from relatively undegassed magmas (Nadeau et al., 1999; Tichomirowa et al., 2006; Zozulya et al., 2007), whereas Sr isotope signatures tend to suggest sub-solidus exchange during late magmatic stages (Tichomirowa et al., 2006). Uranium-Pb isotope data signal the Svecofennian metamorphic overprint and resetting of the Pb–Pb isotope system in apatite at that time (Tichomirowa et al., 2006).

These studies constitute important steps towards the understanding of apatite genesis in the Siilinjärvi Carbonatite Complex. However, apatite is typically characterized by small-scale heterogeneities that reveal the complexity of the processes involved in its formation (e.g., Chakhmouradian et al., 2017; Broom-Fendley et al., 2016, 2017; Decrée et al., 2016, 2020). Thus, a careful petrographic study and in-situ geochemical analyses are needed to document these textural and chemical variations and to better constrain the sequence of processes in the apatite's genesis explaining the variability of P and REE contents observed within the deposit.

This is the aim of the present study in which we conducted (i) a thorough petrographic characterization under cathodoluminescence (CL), which is a useful tool highlighting textures in minerals and their associated geochemical/structural heterogeneities (e.g., Chakhmouradian et al., 2017; Baele et al., 2019), (ii) *in-situ* chemical analyses by electron microprobe analyses (EMPA) and laser ablation-inductively coupled plasma-mass spectrometry (LA-ICP-MS), and (iii) a careful study of the CL and Raman spectra that can help to detect the presence and the level of REE-enrichment in apatite (e.g., Kempe and Götze, 2002; Decrée et al., 2016).

The second objective of this study is to unlock the potential of carbonatite-related deposits for REE recovery. For this purpose, the REE contents of the different lithotypes constituting the Siilinjärvi Complex were determined based on whole rock analyses and laser induced breakdown spectroscopy (LIBS). This became necessary after the few previous studies on the geochemistry of the Siilinjärvi rocks (Puustinen, 1971; Hornig-Kjarsgaard, 1998) had provided incomplete datasets. LIBS provides fast and spatially-resolved, multi-element imaging and constitutes an emerging tool for mineral exploration (Harmon et al., 2019). It is ideally suited for investigating the P and REE distribution in the rocks, irrespective whether or not mineralized.

2. Geological context

The Neoarchean Siilinjärvi Carbonatite Complex is located in the Karelian Province in eastern Finland. The complex forms a roughly subvertical lenticular body that is about 16 km long with a maximal width of 1.5 km (O'Brien et al., 2015, Fig. 1). It was emplaced into Archean tonalite, gneiss, syenite, and quartzdiorite at around 2610 Ma (2610 ± 4 Ma, zircon U–Pb ages, GTK unpublished report in O'Brien et al., 2015; 2613 ± 18 Ma, U–Pb ages on baddeleyite, Bayanova, 2006). A N–S structure likely controlled its emplacement (Puustinen, 1969). Contacts between the Siilinjärvi Carbonatite Complex and the country rocks are either primary magmatic or sheared (O'Brien et al., 2015). Several episodes of deformation affected the Siilinjärvi Carbonatite Complex, including multiphase compressional and metamorphic events related to the Svecofennian orogeny between ~1.9 and 1.7 Ga (Niiranen et al., 2015; O'Brien et al., 2015).

Carbonatite and glimmerite form the central part of the body. The glimmerite-carbonatite series ranges from pure glimmerite (with dominant tetraferriphlogopite) to carbonate glimmerite, silicocarbonatite and carbonatite (with >50 vol% carbonate) (O'Brien et al., 2015). These rock types are intimately mixed, varying from pure glimmerite to pure carbonatite, with carbonate glimmerite and silica carbonatite among intermediate facies (Fig. 2a–e). Most of the carbonatite is present as subvertical veins concentrated towards the center of the intrusion, cutting across glimmerite, whereas glimmerite is located more at the margin of the central core (Puustinen and Kauppinen, 1989; O'Brien et al., 2015). The intrusion of carbonatite magma occurred in several stages (Tichomirowa et al., 2006) and silicocarbonatite formed from later intrusions (Puustinen and Kauppinen, 1989). Carbonatite represents roughly 1.5 vol % of the main intrusion and the final stage of magmatic influx in the system (O'Brien et al., 2015). Tetraferriphlogopite and calcite are the dominant minerals in the glimmerite-carbonatite series. Apatite and richterite are other minerals that are ubiquitous in these lithotypes (Puustinen, 1971; Puustinen and Kauppinen, 1989).

Fenite developed within the country rocks surrounding the glimmerite-carbonatite body and comprises a variety of facies. These are mainly related to the (proportion of) minerals forming the fenites, mostly microcline, amphibole, pyroxene, but also carbonate and quartz (O'Brien et al., 2015). Amphibole-rich fenite (Fig. 2f and g; abbreviated as fenite (amph)) and pyroxene-rich fenite (Fig. 2h and I; abbreviated as fenite (pyrox)) are distinguished. Fenite occurs as megaxenoliths in glimmerite, implying that at least part of the fenite formed early in the history of the complex (O'Brien et al., 2015). According to Poutiainen (1995), fenitization resulted from the circulation of H_2O- and alkali (Na, K)-rich fluids during the pre-emplacement evolution of the carbonatite at mid-crustal conditions.

Ultramafic dikes cut the whole complex (including the fenitized zone) and country rocks. They could also originate from the parental magma of the complex (O'Brien et al., 2015). Based on isotopic evidence, the parent magma of the Siilinjärvi carbonatite and glimmerite was derived from a moderately enriched mantle source (Nadeau et al., 1999; Tichomirowa et al., 2006; Zozulya et al., 2007). Isotope studies further point to an increase of the Sm/Nd ratio of the source domain in the mantle (Tichomirowa et al., 2006), which was also characterized by
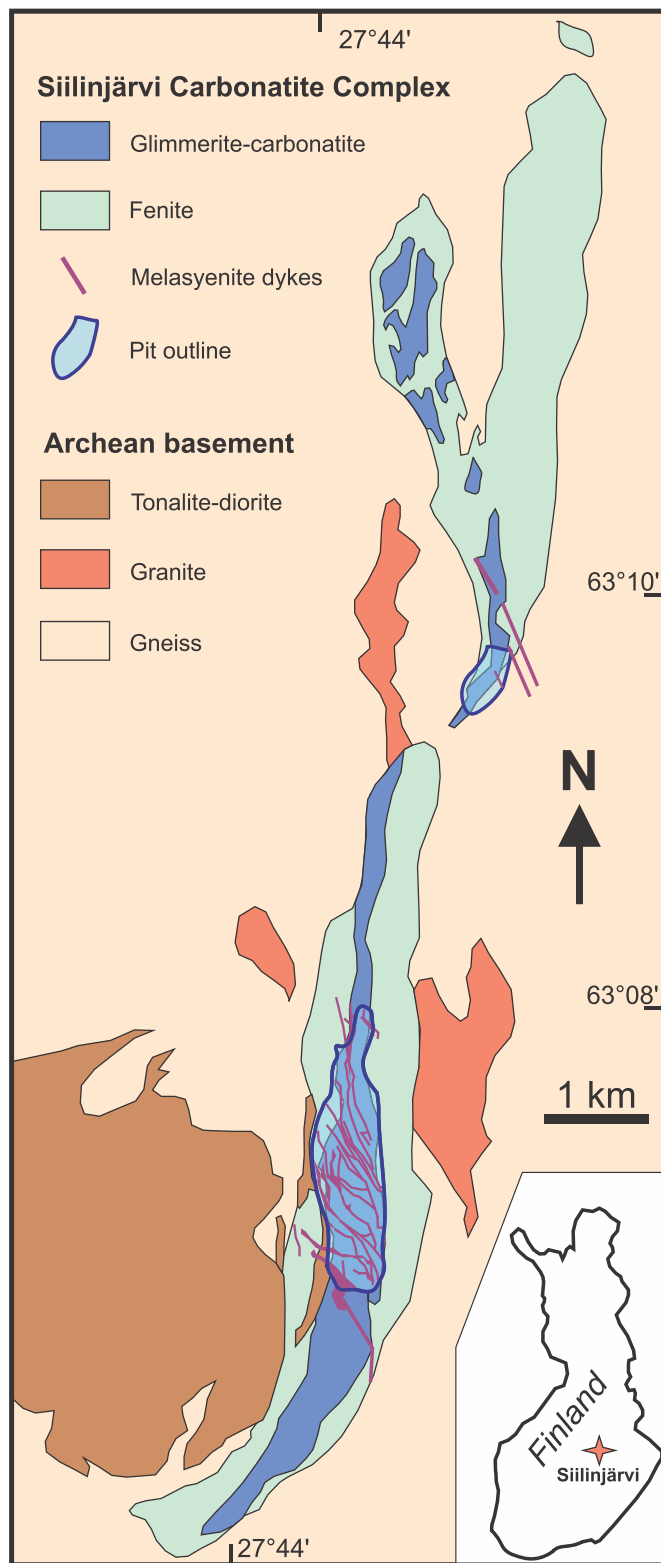
Fig. 1. Geological sketch map of the Siilinjärvi Carbonatite Complex (modified and redrawn from O'Brien et al., 2015). The upper insert shows the location of Siilinjärvi in Finland.

Fig. 2. Selected macrophotographs of Siilinjärvi rocks. (a) Carbonatite with green apatite crystals (sample Si8); (b) Apatite rock made of carbonatite with abundant green apatite crystals (sample Si11); (c) Glimmerite (sample Si9); (d) Silica carbonatite (sample Si7); (e) Carbonate glimmerite (sample Si3); (f) and (g) Amphibole-rich fenite (samples Si6 and Si5); (h) and (i) Pyroxene-rich fenite (samples Si1 and Si10). (For interpretation of the references to color in this figure legend, the reader is referred to the Web version of this article.)

a high $\delta^{13}C$ component during the Archean (Demeny et al., 2004). The magmatic system is thought to have been large and well-mixed. The composition of calcite and apatite further speaks for a moderate level of fractionation of the source magma, which was likely not very REE-enriched (O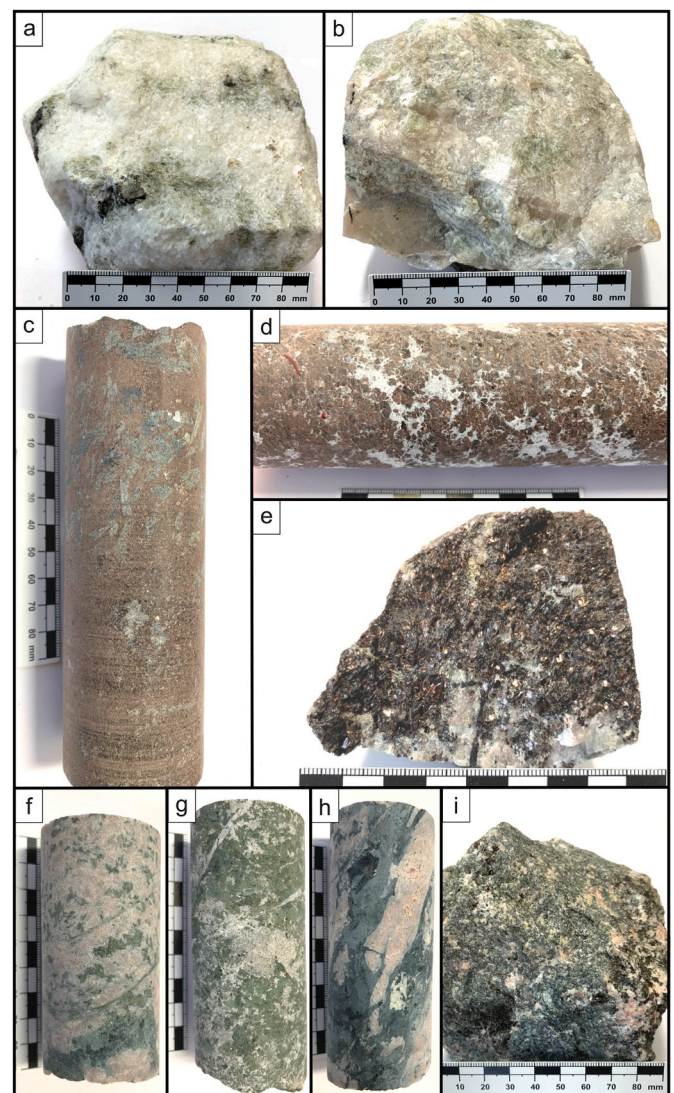'Brien et al., 2015). Strontium isotope data point at sub-solidus exchange with aqueous fluids during emplacement and cooling of the carbonatites (Tichomirowa et al., 2006). Further perturbation of the isotopic systems was induced by the Svecofennian orogeny, which caused resetting of the isotope systems (Tichomirowa et al., 2006), in spite of a rather low grade of metamorphism (Puustinen and Kauppinen, 1989).

3. Material and methods

Eleven samples were taken from the Siilinjärvi mine (Table 1). The petrographic analysis was based on optical microscopy and scanning electron microscopy (SEM) using a Quanta 20 ESEM (FEI), with energy-dispersive spectroscopy (Apollo 10 Silicon Drift EDS detector; EDAX) at the Royal Belgian Institute of Natural Sciences (RBINS). Cathodoluminescence (CL) studies were performed at the University of Mons (UMONS) using a cold-cathode CL unit model Mk5 operated at 15 kV beam voltage and 500 µA current (Cambridge Image Technology Limited). The surface area of the unfocused electron beam on the sample

Table 1
Succinct description of all examined samples from the Siilinjärvi Carbonatite Complex.

Sample	Ref. drill core (if available)	Description
Si1		fenite (amph)
Si2	R713 L-114 513.95–514.45	fenite (amph)
Si3		carbonate glimmerite
Si4		fenite (pyrox)
Si5		fenite (pyrox)
Si6		fenite (pyrox)
Si7	UCS R713 L-128 577–577.60	silica carbonatite
Si8		carbonatite
Si9	UCS R713 L-136 614.85–615.35	glimmerite
Si10		fenite (amph)
Si11		carbonatite (apatite rock)

was 12×4 mm, resulting in a current density of about 10 μA/mm^2. CL spectra were recorded with a CITL optical spectrometer model OSA2 allowing acquisition from 350 to 1100 nm at 3.7 nm spectral resolution. Spectra were acquired and processed using Spectragryph optical spectroscopy software (https://www.effemm2.de/spectragryph/). A dark spectrum, i.e. a spectrum of the stray light in the CL chamber, was systematically subtracted from the experimental spectrum. However, this procedure was not always successful in suppressing the two artifact peaks that are sometimes observed on both sides of the Eu^{2+} emission around 410 nm. These artifact peaks, which sometimes appear negative due to over-correction, are due to the spurious emission of some excited species (probably nitrogen) from the atmosphere in the electron gun. Spectral CL images of the Nd^{3+} emission were collected by inserting an optical bandpass filter with a transmission curve centered at 880 nm and 50 nm wide (full width at half maximum) in the light path. Such spectral CL imaging enhances the details of the distribution of the apatite activated by light REE, which is especially useful when apatite luminescence is overwhelmed by the intense luminescence of calcite and feldspars. In addition, Nd^{3+} emits in the near infrared region of the spectrum and is therefore not visible in color CL images. Raman spectroscopy was performed at the Royal Belgian Institute of Natural Sciences to investigate the fluorescence induced by the REE. We used a 785 nm (red) laser Raman spectrometer (Senterra, Olympus BX51, Bruker optics). The spectra were acquired using a 1 mW excitation power, 5×30 s integration time and with a 50 μm spectrometer slit. They were processed using Spectragryph optical spectroscopy software. The Raman shift has been transformed into wavelengths according to the following formula: Wavelength (nm) = (Laser wavelength^{-1} - Raman shift x 10^{-7})$^{-1}$. Here, the laser wavelength is 785 nm and the Raman shift is given in cm^{-1}.

Laser-Induced Breakdown Spectroscopy (LIBS) was performed with a system under development at UMONS, which comprises a flashlamp-pumped Q-switched Nd:YAG laser (Quantel-Lumibird QSmart 450, France) with frequency doubling and quadrupling crystals (266 nm wavelength) and a 9-channel optical CCD spectrometer with integrated delay electronics (Avantes ULS2048, The Netherlands). The spectral range and resolution of the spectrometer were 190–1100 nm and 0.05–0.2 nm (from ultraviolet to infrared), respectively. LIBS maps were recorded by moving the sample with a motorized XY stage (Zaber Technologies, Canada) that was synchronized with the laser Q-switch using a digital pulse/delay generator (Quantum Composers, USA). The surface of the sample was ground on an ultra-flat lapping plate using grit 600 silicon carbide abrasive in order to achieve a flat surface with an even rugosity. A constant lens-to-sample distance, which is critical in LIBS spectroscopy, was ensured by finely adjusting the horizontality of the surface using laser pointers. Laser pulse duration and energy were 5 ns and 15 mJ, respectively. The laser pulses were focused onto the sample surface with a 150 mm focal distance silica planoconvex lens. With these settings, the diameter of the ablation craters was about 200 μm, which yields a fluence of 48 Jcm^{-2} and an irradiance (power density) of 9.5 GWcm^{-2}. The plasma light was collected by a 6 mm focal

distance planoconvex lens and injected into multi-furcated optical fibers connected to the spectrometer. The delay between laser shots and start of the integration was 1 μs to avoid the intense initial continuum radiation of the plasma and the integration time was set to 1 ms. The energy of the laser pulses was continuously monitored by sampling the beam with a silica window and measuring the energy with a pyroelectric sensor (Thorlabs ES220C). The measured relative standard deviation of pulse energy fluctuation at 10 Hz repetition rate was found to be 4.1% after thermal stabilization of the frequency-quadrupling crystals. Acquisition and processing of the LIBS spectra were achieved with Spectragryph spectroscopy software. Jython and Java scripting under Fiji/ImageJ free image analysis software (Rueden et al., 2017) were used to build the hyperspectral data cube and to extract the LIBS maps. Elemental lines were identified based on both experimental LIBS spectra of internal reference materials and the NIST atomic emission database. The LIBS maps show the intensity of selected ionic (II), atomic (I) or molecular emission lines without calibration. Therefore, they are qualitative geochemical maps. The following emission lines were used for the LIBS maps presented in this study: Ca I (458.59 nm), Si I (390.55 nm), P I (255.33 nm), CaF (~543 nm), Na I (819.48 nm), K I (766.49 nm), La II (412.32 nm) and Ce II (416.46 nm). The selection of the wavelengths was based on the following criteria: maximizing intensity while avoiding those lines that obviously suffer from autoabsorption and minimizing interference from other elements. The CaF molecular emission is a good means of detecting F because this element is extremely difficult to excite under common experimental LIBS conditions due to its very high first ionization potential. However, when Ca is present together with F, both elements form a transient CaF molecule in the plasma as it cools and the associated intense emission band is easily detected. The only drawback of this method is that fluorine is not detected if no Ca is present in the sample, which could, however, be mitigated by nebulizing some Ca solution into the plasma (Alvarez Llamas et al., 2017).

In all the samples zoned apatite grains were investigated in-situ for their composition. Where possible, the different types of analyses (EMPA and LA-ICPMS) have been performed on the same spot or nearby spots. Quantitative microanalyses of the chemical composition for major elements (Table 1S (Supplementary Material)) were acquired using a JEOL JXA 8800L electron microprobe at the Institute of Geography and Geology, University of Würzburg (Germany). It was operated at 15 kV and 4 nA, with a beam diameter of 10 μm. This microprobe is equipped with four wavelength-dispersive (WDS) spectrometers and standard LDE1, TAP, PET and LIF crystals (LiF for F, Fe$_2$O$_3$ for Fe, SrSO$_4$ for Sr, MnTiO$_3$ for Mn, MgO for Mg, BaSO$_4$ for S and Ba) and mineral standards (albite for Na, vanadinite for Cl, apatite for P and Ca, and andradite for Si) supplied by CAMECA (SX Geo-Standards) were used as a reference. The Lα line was used for the measurements of Sr and Ba, and the Kα line for all other elements. The lower limit of detection is typically better than 0.05 wt%. For each mineral spot, the relatively mobile elements F and Na were analyzed first in order to prevent their potential loss over the course of the analysis. The analytical data acquired are provided in Table 1S (Supplementary Material). A correction for excess F due to third-order interference of P Kα on F Kα was applied. Excess F was estimated at about 0.35% based on 15 measurements of F Kα in a phosphate that does not contain F (reference monazite at Univ. Würzburg). The measurements yielded a mean of 0.040% "fake" F per % P. A similar value (0.045%) was obtained by Potts and Tindle (1989). Note that grain orientation and anisotropic ion diffusion can also have a substantial influence on the quantification of F with the electron microprobe (e.g., Stormer et al., 1993; Goldoff et al., 2012). For the compositional maps of apatite grains, an acceleration voltage of 15 kV and a beam current of 40 nA were used with a spot size of 5 μm.

Laser ablation inductively coupled mass spectrometry (LA-ICPMS) was performed at GeoRessources (Nancy, France), with a GeoLas excimer laser (ArF, 193 nm, Microlas) coupled to a conventional transmitted and reflected light microscope (Olympus BX51) for sample observation

and laser beam focusing onto the sample and an Agilent 8900 triple quadrupole ICP-MS used in no-gas mode. The LA-ICPMS system was optimized to have the highest sensitivity for all elements (from 7Li to 238U), ThO/Th ratio < 0.5% and Th/U ratio of ~1. Samples were ablated with a laser spot size of 32 μm to avoid mixing between the different zones observed in the apatite crystals. A fluence of ~7 J cm^{-2} and a repetition rate of 5 Hz were used. The carrier gas used was helium (0.45 l/min) which was mixed with argon (0.5 l/min) gas before
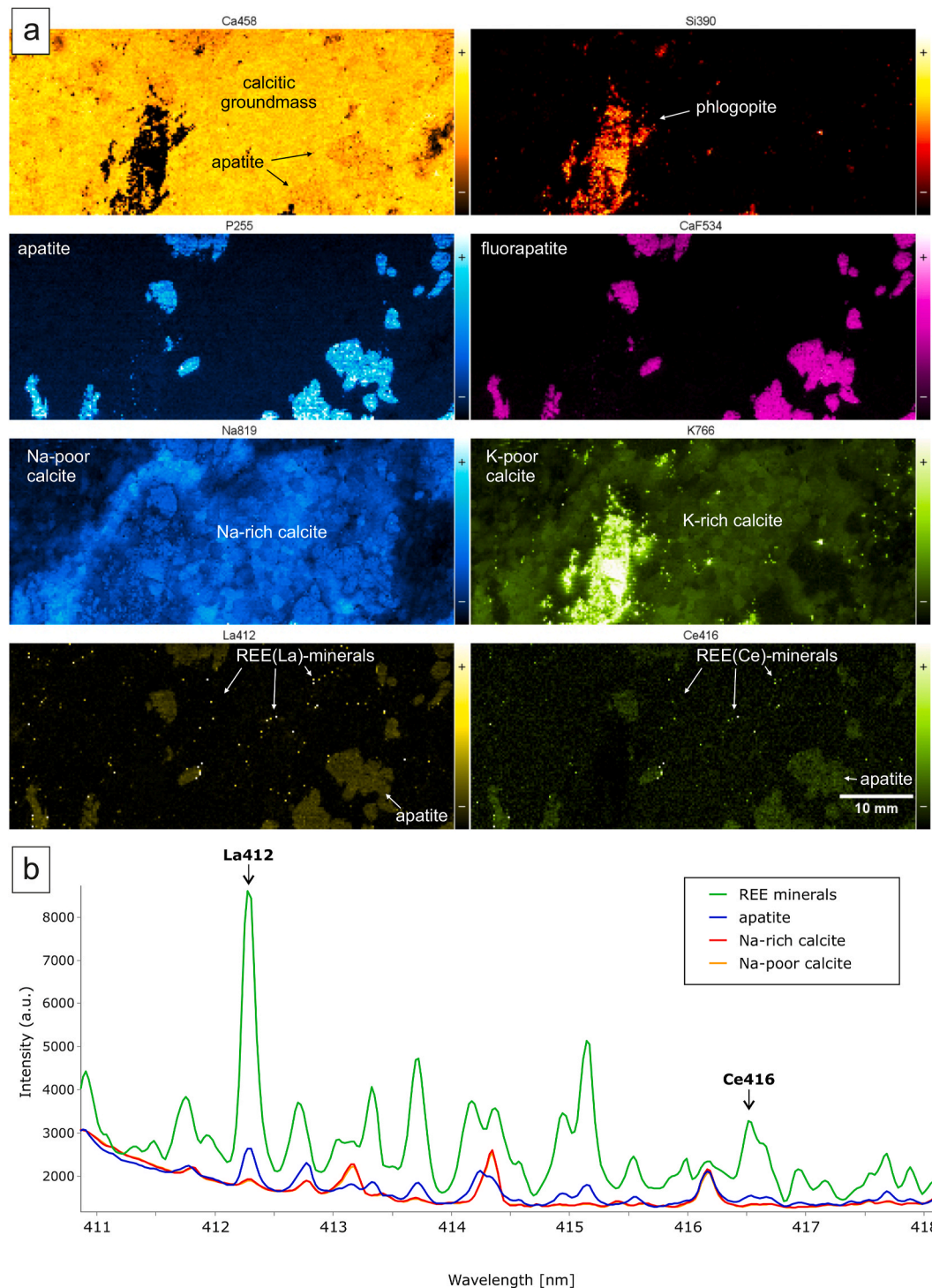

Fig. 3. LIBS analysis of an apatite rock (apatite-rich carbonatite, sample Si11) from Siilinjärvi. Element names are followed by the integer part of the emission wavelength that was used. (a) Selected LIBS maps that show the distribution of both the major minerals (calcite, phlogopite and fluorapatite, as inferred from the distribution of Ca, Si, P, CaF, K and other elements not shown here) and minute REE-minerals (as inferred from the bright spots in La and Ce maps). Although REE are detected in apatite, REE-minerals are scattered throughout the matrix but not included in apatite nor in phlogopite. The map of molecular CaF emission confirms the apatites are all fluorapatites. Note the Na- and K-rich zone within the calcitic groundmass of the carbonatite. (b) Example LIBS spectra of the 411–418 nm range showing the REE lines that were used for mapping elements in the carbonatite sample shown in (a). Each spectrum was obtained by averaging several spectra by selection of a ROI (Region Of Interest) on the maps. The spectra of Na-Poor and Na-rich calcite are identical (except for Na and K, whose emission peaks are observed outside the displayed wavelength range).

entering the ICP-MS. The ICP-MS settings were the following: ICP RF Power at 1550 W, cooling gas (Ar) at 15 l/min, auxiliary gas (Ar) at 0.97 l/min, make-up gas (Ar) at 0.5 l/min and dual detector mode was used. For each analysis, acquisition time was 30 s for background, 40 s for external standards (NIST SRM 610, NIST SRM 612 and NIST SRM 614 silicate glasses (Jochum et al., 2011 for concentrations)) and 40–50 s for apatite. The analytical procedure for the two sessions was the following:

2 analyses of NIST SRM 614, 2 analyses of NIST SRM 612, 2 analyses of NIST SRM 610, analyses of the apatites (series of ~20 analyses separated by the analysis of a series of 1 NIST SRM 614, 1 NIST SRM 612 and 1 NIST SRM 610), 2 analyses of NIST SRM 614, 2 analyses of NIST SRM 612 and 2 analyses of NIST SRM 610. The external standard was NIST SRM 610 and ^{44}Ca was used as internal standard. NIST SRM 614 and NIST SRM 612 silicate glasses were analyzed and considered as
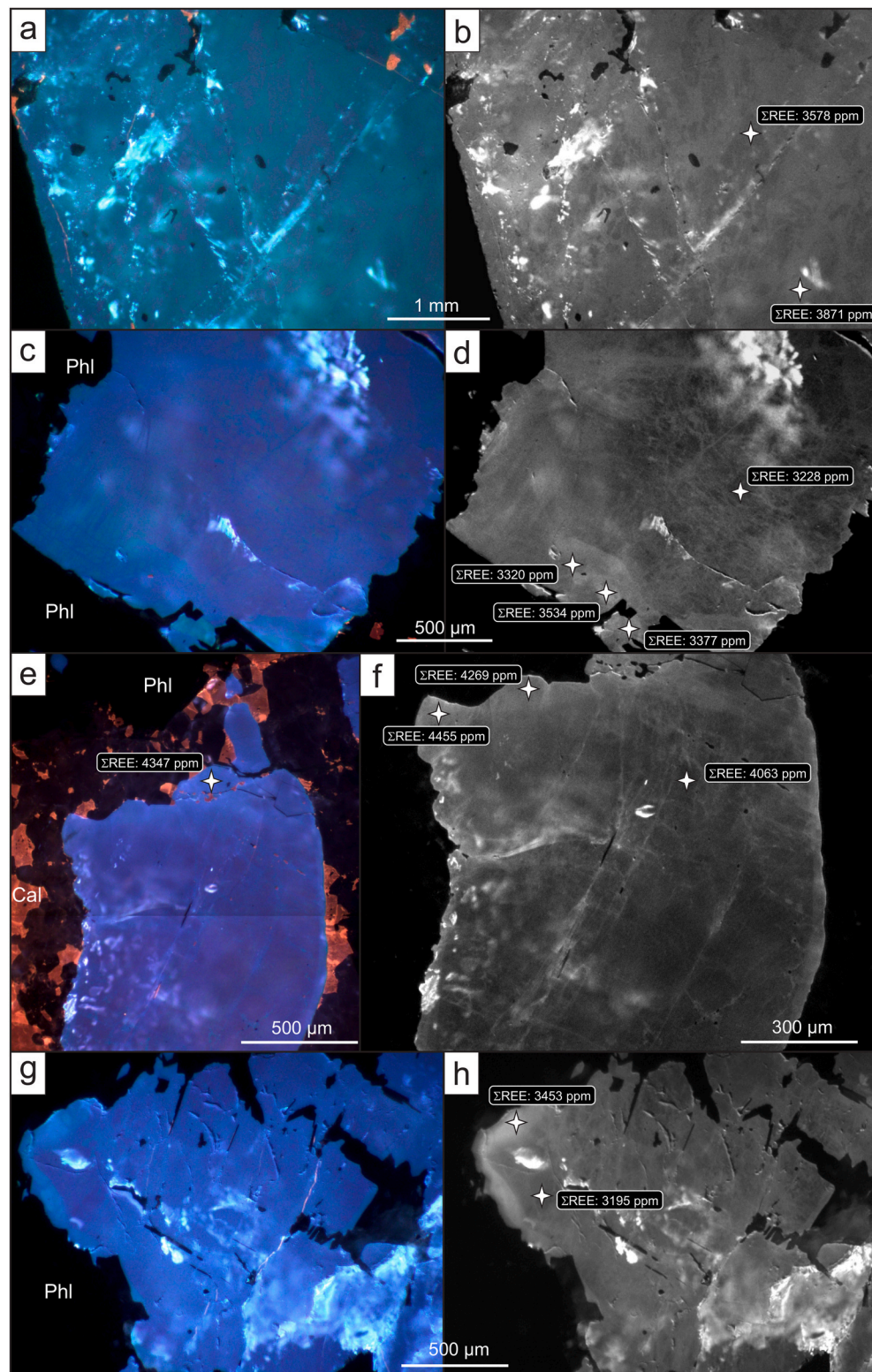

Fig. 4. Cathodoluminescence (CL) photomicrographs of the Siilinjärvi glimmerite-carbonatite series. Color CL in (a),(c),(e) and (g). Spectral CL (Nd^{3+} emission filtered at 880 nm) in (b),(d),(f) and (h); Cal - calcite, Phl - tetraferriphlogopite. The four-pointed stars represent the spots where EPMA and LA-ICPMS analyses were performed. Related REE content (ΣREE in ppm) is indicated in a black box. (a–b) Apatite crystal in apatite rock (sample Si11) exhibiting a heterogeneous texture; a blue-luminescent apatite is partly altered/replaced by a green-luminescent apatite, which is characterized by a stronger Nd activation; (c–d) Green-luminescent apatite replacing a blue-violet-luminescent apatite towards the outer part of a crystal hosted by a glimmerite. Nd activation increase accordingly towards the crystal rim, suggesting a higher concentration in LREE (sample Si9); (e–f) Violet-luminescent apatite with a more bluish luminescence in the crystal rim and along fissures. These bluish zones correspond to an increased Nd-activation (silica carbonatite, sample Si7); (g–h) Closely-packed cluster of blue-violet-luminescing with more bright/greenish luminescence in the rim of some crystals. Replacement zones inside the grains also present this brighter luminescence. The latter corresponds to a higher Nd activation (carbonate glimmerite, sample Si3). (For interpretation of the references to color in this figure legend, the reader is referred to the Web version of this article.)

cross-calibration samples to control the quality of the analyses (precision, accuracy, repeatability) and to correct the possible drift during the analytical session. The Ca contents in apatite were measured before LA-ICP-MS analyses using an electron microprobe (Cameca SX-50, University of Würzburg, Germany), to check the overall homogeneity of the apatite grains. A Ca concentration of 39.54 wt% was used for internal standardization. The following isotopes were measured: ^{29}Si, ^{44}Ca, ^{45}Sc, ^{51}V, ^{85}Rb, ^{88}Sr, ^{89}Y, ^{90}Zr, ^{93}Nb, ^{137}Ba, ^{139}La, ^{140}Ce, ^{141}Pr, ^{146}Nd, ^{147}Sm, ^{153}Eu, ^{157}Gd, ^{159}Tb, ^{163}Dy, ^{165}Ho, ^{166}Er, ^{169}Tm, ^{172}Yb, ^{175}Lu, ^{178}Hf, ^{181}Ta, ^{208}Pb, ^{232}Th, ^{238}U. Acquisition times were 0.01 s for all the isotopes except rare earth elements, which were measured with 0.02 s. Total cycle time was 531 ms. The precision was better than 10% for all the rare earth elements. Data treatment was done using the software "Iolite" (Paton et al., 2011), following Longerich et al. (1996) for data reduction. Data are provided in Table 2S (Supplementary Material).

Finally, major and trace element analyses (Tables 3S and 4S (Supplementary Material)) were carried out on the 11 samples at the Laboratoire G-Time (ULB). For measuring the major and trace element contents, ~50 mg of powdered samples were melted by alkaline fusion after adding 0.8 g of lithium metaborate and 0.2 g of lithium tetraborate in a graphite crucible. After 5 min at 1000 °C, the beads were redissolved in a stirring solution of HNO_3. Major elements were measured on the ICP-OES Thermofischer Scientific iCAP at ULB, using Y as internal standard. Two USGS standards were used (BHVO-2 and AGV-2) and the total reproducibility was better than 2% for each element. Loss on ignition was measured on a 0.5 g aliquot after 5 h at 800 °C. Trace elements were measured on an Agilent 7700 ICP-MS, also at ULB, by adding In as internal standard. The same USGS standards were used. The total reproducibility was systematically better than 5%.

4. Results

4.1. Petrography

4.1.1. Apatite in glimmerite and carbonatite

In rocks of the glimmerite and carbonatite series (including silica carbonatite and carbonate glimmerite), apatite is mostly present as isolated elongated euhedral to anhedral crystals (from about 1 mm to a few centimeters in size) or as clusters of crystals (Figs. 3 and 4).

In these lithotypes, apatite is mostly associated with tetraferriphlogopite and calcite in variable proportions. K-feldspar, clinopyroxene and amphibole (richterite) are also locally abundant. REE are concentrated in mm-to cm-sized apatite crystals and small (<200 μm) REE-rich grains that are scattered in the carbonatite matrix but not included within apatite (see LIBS image and spectra of the apatite rock ore; Fig. 3a and b). In the apatite-rich carbonatite (exploited in the Siilinjärvi mine, sample Si11), apatite seems to be associated with a conspicuous Na- and K-rich zone within the carbonatite matrix, which could be related to a separate carbonatite generation (see Fig. 3). The blue luminescence of apatite is dominant in the observed facies (Fig. 4a,c,e, g). The link between a CL color and activation by a specific element can be deduced from cathodoluminescence spectra (Fig. 7a–c). This blue CL color is due to REE activation, mostly Eu^{2+} (e.g., Marshall, 1988; Mitchell et al., 1997; Blanc et al., 2000; Kempe and Götze, 2002; Mitchell et al., 2014, 2020). A stronger activation by Sm^{3+} produces violet shades in the earliest zones (cores) of the crystals (Fig. 4c,e,g), whereas Dy^{3+} induces greenish shades (as illustrated in cathodoluminescence spectra; Fig. 7a). The Nd^{3+} emission lines (multiplet in the 850–930 nm range) are well visible when the Raman shift is converted back to the absolute emission wavelength. This method, already used by Decrée et al. (2016), makes it possible to directly compare REE fluorescence (here Nd^{3+}) with cathodoluminescence (Fig. 7d).

In the glimmerite-carbonatite series, apatite shows a range of CL colors, with violet CL within early-formed cores to greenish CL inside later generations. In the apatite rock (an apatite-rich carbonatite, sample Si11), a blue-green-luminescent apatite replaced massively a blue-violet apatite as a dense network (Fig. 4a). The greenish CL is accompanied with an increase in Nd^{3+} activation (Fig. 4b). In glimmerite, silica carbonatite and carbonate glimmerite, this replacement occurs preferably along the walls of fissures and cleavage planes. Replacement or overgrowth at the rim of apatite crystals are also commonly observed (Fig. 4c,e,g). The green CL is again coupled with an increase in Nd activation from early-to late-formed apatite (Fig. 4d,f,h).

4.1.2. Apatite in fenite

In the fenite, apatite is mostly present as stubby anhedral crystals (a few hundreds of micrometers in size; Fig. 5) associated with a mineral paragenesis comprising K-feldspar, amphibole (actinolite), clinopyroxene (aegirine-augite), calcite and albite. Minor phases are magnetite and REE-minerals (britholite and monazite). The latter are preferentially clustered in the vicinity of apatite crystals (see LIBS image; Fig. 6). Red luminescence of K-feldspar (Fig. 5a) is due to Fe^{3+}-activation. This is common in feldspars from fenitized rocks (Marshall, 1988). As mentioned for the apatite in the glimmerite-carbonatite series, the blue, violet-reddish and greenish CL of apatite in fenite (Fig. 5a,c,e) are related to activation by Eu^{2+}, Sm^{3+} and Dy^{3+}, respectively (see cathodoluminescence spectra, Fig. 7b and c). A notable exception is a bright green-luminescent apatite observed in a pyroxenite-rich fenite. Spectroscopic data show that this apatite is Mn^{2+}-activated, as illustrated by its intense broad band emission centered at about 570 nm in cathodoluminescence spectra (Fig. 7b). As for apatite hosted by glimmerite and carbonatite, transformed Raman spectra emphasize the role of Nd^{3+}-induced fluorescence/luminescence in these rocks (Fig. 7e and f).

Whether it is in pyroxenite- or amphibole-rich fenite, apatite always shows a complex texture under CL. Its luminescence is blue-violet in the primary apatite with irregular blue-green-luminescent zones highlighting replacement (Fig. 5a,c) or overgrowth, locally after corrosion/resorption of the primary apatite (as the green-luminescent rim in Fig. 5a,e). Replacement and overgrowth zones are mostly characterized by a stronger Nd-activation compared to early-formed apatite (Fig. 5b, d). In contrast, in several pyroxenite-rich samples (Si5 and Si6), bright green and dark green-luminescent rim and outer replacement zones of apatite grains are associated with a strong decrease in Nd activation (Fig. 5e–g) and REE contents (the decrease in Ce is illustrated in Fig. 5g). Locally, britholite is found lining these grains (Fig. 5h). Note that these episodes of overgrowth/replacement with contrasting chemistry can occur in successive phases, with first the deposition of a blue-luminescent apatite (with strong Nd-activation) after a violet-luminescent core, before an overgrowth of a more greenish apatite that is overall less activated by Nd^{3+} (Fig. 5c and d).

4.2. Mineral chemistry

Apatite from Siilinjärvi shows a large range of CaO (50.96–55.77 wt %) and P_2O_5 concentrations (38.04–42.43 wt%, see Table 1S (Supplementary Material)). These analyses suggest that substitutions (with F, Si, Sr and REE, for instance; Pan and Fleet, 2002) are significant at Ca and P sites.

Fluorine contents range from 2.34 to 3.35 wt% (which are below the theoretical maximum of 3.73 wt% in apatite), whereas Cl contents are always below the detection limit (<0.05 wt%). The SiO_2 and SO_3 contents are low to moderate (≤0.14 wt%). Strontium oxide contents vary between 0.61 and 1.20 wt%, whereas FeO (≤0.16 wt%) and Na_2O (≤0.25 wt%) contents are low to moderate. Barium oxide and MnO contents do not exceed 0.09 wt% and 0.12 wt%, respectively. Magnesium oxide content is above the detection limit (0.07 wt% MgO) in only four analyses.

The analyzed apatite grains display similar slightly curved chondrite-normalized REE patterns in general (Table 2S (Supplementary Material)), except those hosted by two pyroxene-rich fenite (Fig. 8a–d). Apatite from the glimmerite-carbonatite series has high total REE
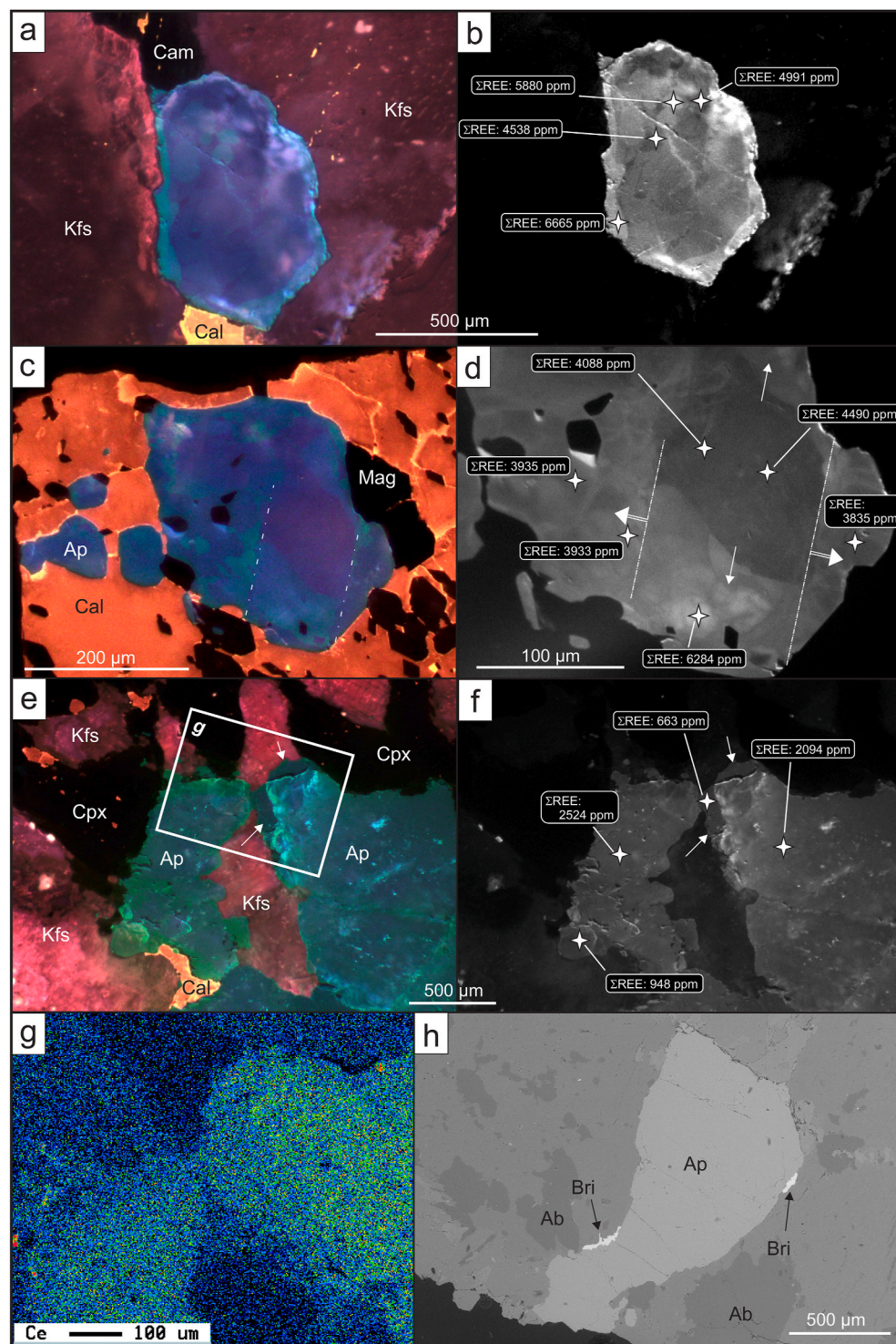
Fig. 5. Cathodoluminescence (CL) (a–f), EPMA (g) and backscattered electron (h) photomicrographs of the Siilinjärvi fenites. Color CL in (a), (c) and (e). Spectral CL (Nd^{3+} emission filtered at 880 nm) in (b), (d), (f) and (h); Ab-albite, Ap-apatite, Bri-britholite, Cal - calcite, Cam-clinoamphibole, Cpx-clinopyroxene, Kfs - K-feldspar, Mag – magnetite, Phl - tetraferri-phlogopite. The four-pointed stars represent the spots where EPMA and LA-ICPMS analyses were performed. Related REE content (ΣREE in ppm) is indicated in a black box. (a–b) Zoned apatite crystals with a blue-violet CL core and green CL rim in a pyroxene-rich fenite (sample Si4); textures suggest the partial replacement of the early-formed (violet-luminescent) grain by an apatite with stronger Nd-activation; (c–d) Stubby crystal of apatite in an amphibole-rich fenite (sample Si10). Apatite exhibits a complex luminescence texture. The primary blue-violet-luminescent apatite is partly replaced by light-blue-luminescent apatite (with increased Nd-activation), likely along the direction indicated by the single arrow. It is then overgrown by apatite with a lower Nd activation; (e–g) Closely-packed cluster of apatite crystals in a pyroxene-rich fenite (sample Si5); apatite rim is characterized by a bright green CL, while apatite overgrowth (indicated by arrows) shows a dark blue-greenish luminescence. Interestingly, both are characterized by a decrease in Nd-activation (f) and a decrease in Ce (g), highlighting a global decrease of REE content. The white square presented in (e) corresponds to the zone illustrated in (g); (h) Britholite overgrowth on an apatite grain in a pyroxene-rich fenite (sample Si6). (For interpretation of the references to color in this figure legend, the reader is referred to the Web version of this article.)

contents (3195–6665 ppm), with a strong enrichment in LREE (La_N/Yb_N = 97–129) and a slightly negative Eu anomaly (0.82–0.87; Fig. 8a and b).

Similar trends are observed for apatite from several studied fenite samples (samples Si4 and Si10). In the latter, apatite exhibits REE and LREE enrichment (ΣREE = 3835–6665 ppm; La_N/Yb_N = 97–200), with a negative Eu anomaly of about 0.82–0.86 (Fig. 8c; Table 2S (Supplementary Material)). Apatite in other fenite samples is generally less rich in REE and LREE (La_N/Yb_N = 12–103; ΣREE = 663–4567), with a more significant negative Eu anomaly (Eu/Eu* = 0.73–0.84). The most

extreme values (low La_N/Yb_N, low ΣREE and significant negative Eu anomaly) were measured in apatite that is hosted by two pyroxene-rich fenite (Fig. 8d). The corresponding REE patterns are moderately curved (Fig. 8d).

The primitive mantle (PM)-normalized spidergrams (Fig. 9a) highlight this enrichment in REE and the depletion in Pb, V and high-field-strength elements (HFSE), i.e. Nb, Ta, Hf and Zr. These latter are, however, less depleted in the fenites. The same trends are overall observed when apatite analyses are normalized to their P_2O_5 content (as determined by EMPA analyses; Fig. 9b). A notable difference is the
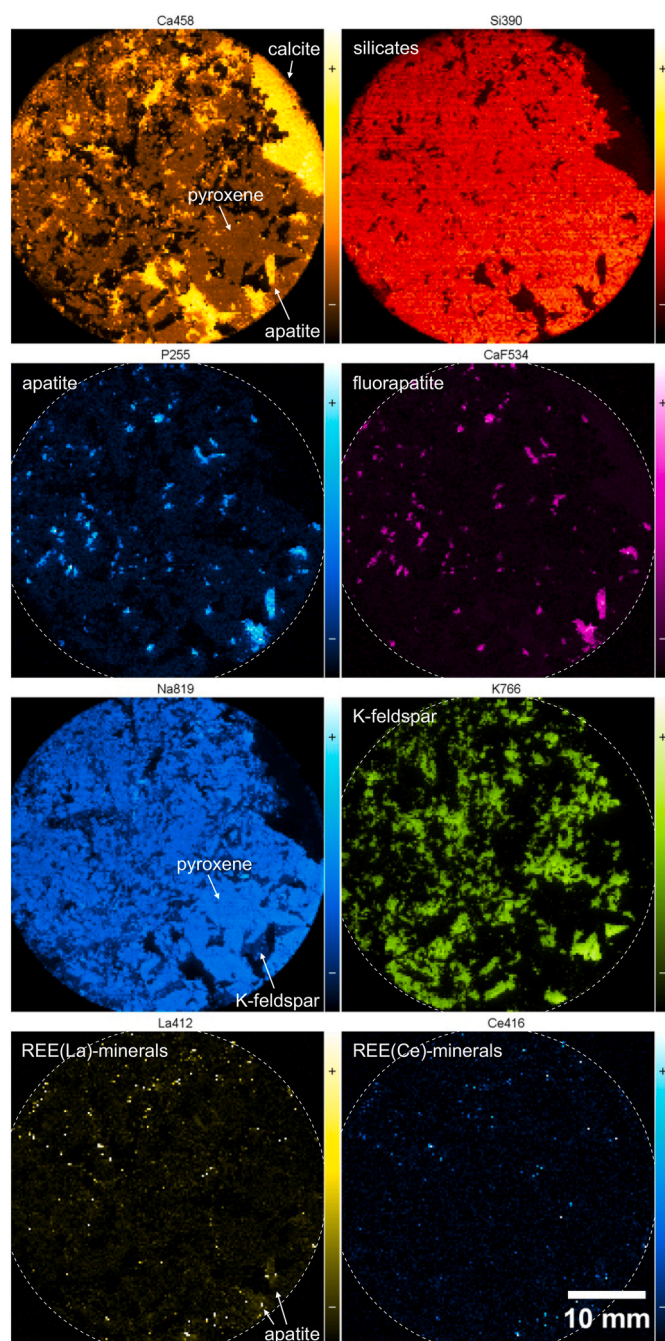
Fig. 6. Selected LIBS maps of a 38 mm diameter core of pyroxene-rich fenite from Siilinjärvi (sample Si 1). Elements names are followed by the integer part of the emission wavelength that was used. Here, La and Ce maps do not exactly match together as in the carbonatite, suggesting a more diverse REE-mineral assemblage.

relative enrichment in Pb compared to U and Th.

Geochemical intra-grain variability can be important in apatite, consistent with the complex texture revealed by Nd^{3+} emission under CL. A correlation between CL intensity/color and REE content is observed in most of the samples. In the glimmerite-carbonatite series, the early-formed violet-blue-luminescent apatite (or apatite core) is less enriched in REE than the blue-green-luminescent rims and alteration zones (Fig. 8a and b). Similar correlations are also observed in pyroxene- and amphibole-rich fenite (samples Si2 and Si4; Fig. 8c and d). By contrast, (dark) green-luminescent overgrowths/rims in apatite from other pyroxene-rich fenite samples are significantly depleted in (L)REE

compared to the violet-luminescent early-formed apatite (samples Si5 and Si6; Fig. 8d). Finally, apatite hosted by amphibole-rich fenite (samples Si1 and Si10; Fig. 8c) shows more complex textures, with (i) an early enrichment in REE compared to the violet-luminescent core; this enrichment is overall correlated with a blue luminescence of apatite; and (ii) secondary overgrowth (or replacement) by a greenish-luminescent apatite is characterized by a slight decrease in REE (Fig. 8c).
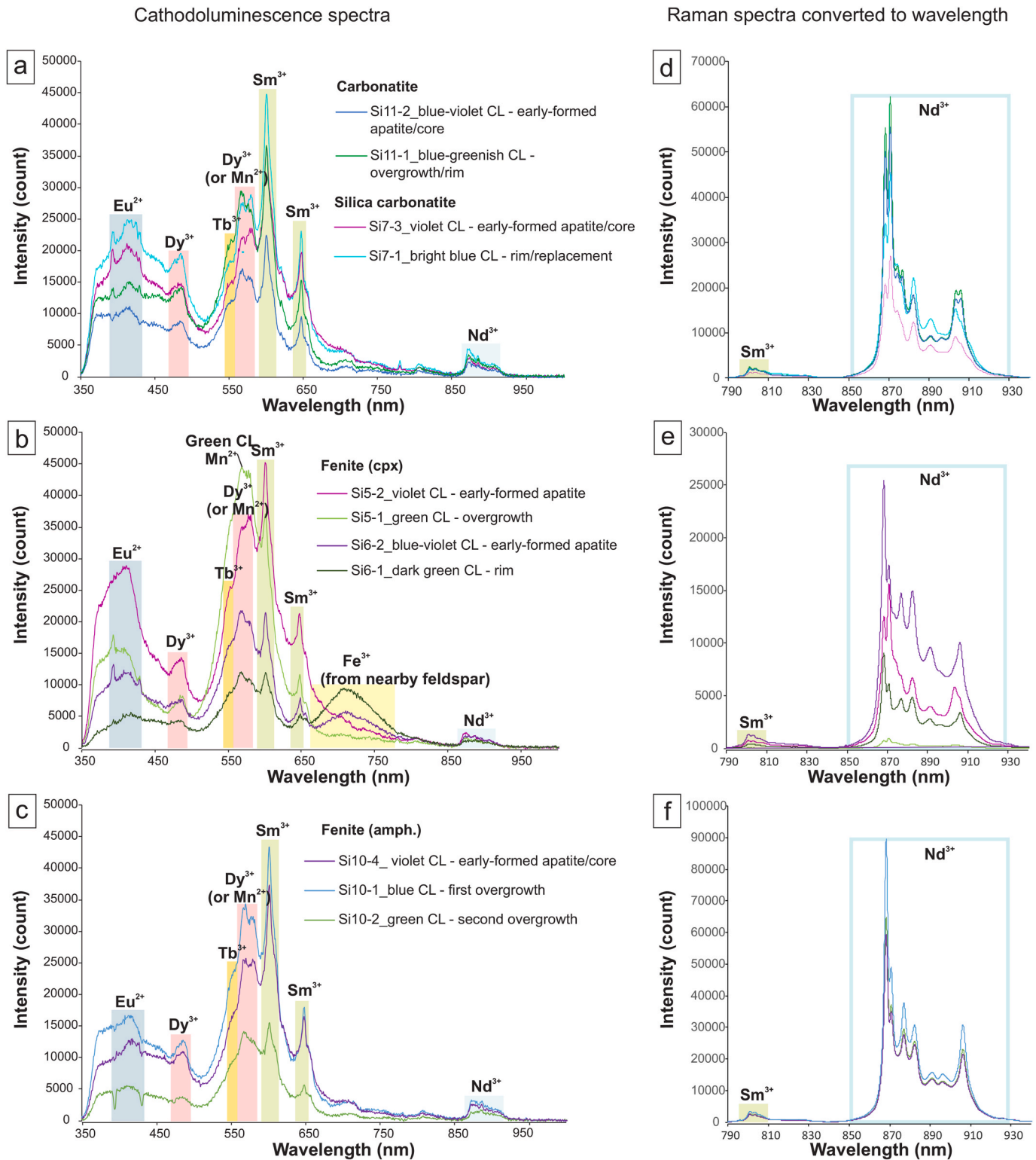
4.3. Whole rock chemistry

The analyzed carbonatite has a CaO content of about 54.5 wt% (54.09 and 54.69 wt%), with little MgO (~1 wt%). The P_2O_5 contents vary between 11.42% in a typical carbonatite and can reach 34.18 wt% in a portion of the carbonatite body that can be considered an apatite rock (Table 3S (Supplementary Material)). In the other rocks pertaining to the glimmerite-carbonatite series, the P_2O_5 content ranges from 0.23 wt% (in the carbonate glimmerite) to 14.01 wt% (in the glimmerite), and 2.32 wt% in the silica carbonatite. The CaO content is strongly variable (from 4.10 to 18.60 wt%) in glimmerite-carbonatite. These rocks are rich in SiO_2 (27.24–36.94 wt%), MgO (14.92–21.51 wt%), Fe_2O_3 (6.96–9.91 wt%), Al_2O_3 (5.32–8.07 wt%) and K_2O (4.91–6.89 wt%). All other element contents are below 1 wt%.

Some fenite samples are slightly enriched in phosphates (0.55–2.95 wt% P_2O_5) and contain mainly silicates (44.97–56.77 wt% SiO_2). The content in the other major elements varies significantly, with 3.73–12.87 wt% Al_2O_3, 6.39–19.08 wt% CaO, 2.68–11.34 wt% Fe_2O_3 and 2-67-10.61 wt% MgO. They also contain a few percent of Na_2O and K_2O (2.01–3.66 wt% and 2.02–7.66 wt%, respectively). One of the amphibole-rich fenites contains more carbonates (sample Si10). Its SiO_2 content is consequently lower (26.65 wt%), as are the other major elements apart from CaO (28.03 wt%), MgO (11.77 wt%) and Fe_2O_3 (5.68 wt%).

The chondrite-normalized REE patterns of rocks of the glimmerite-carbonatite series (Fig. 10a) show an enrichment in LREE (La_N/Yb_N from 60 to 119), with high ΣREE contents (396–3176 ppm) and low negative Eu anomalies (0.90 < Eu*/Eu < 0.93). An exception is the carbonate glimmerite, which contains only 0.23 wt% P_2O_5 and is also particularly poor in REE (68 ppm in total). Though displaying similarly shaped REE patterns, the fenites are in general less enriched in REE and LREE (116< ΣREE <454 ppm; 22< La_N/Yb_N < 85), with low negative Eu anomalies (0.86 < Eu*/Eu < 0.95). A notable feature shared by a few samples of the glimmerite-carbonatite series and fenites is an enrichment in the heaviest REE (Yb–Lu). The shape of these REE patterns is overall similar to those obtained on apatite (LA-ICPMS measurements; Fig. 10a). Moreover, a good positive correlation between the total REE content and the P_2O_5 content indicates that apatite is an important REE-host (Fig. 10b).

The primitive mantle (PM)-normalized spidergrams for the Siilinjärvi carbonatite (Fig. 10c) display an enrichment in REE (which is quite similar to that measured in-situ in apatite) and several large-ion lithophile elements (LILE), such as Sr, Ba and Th, but a depletion in K, Ti, V. The contents of other HFSE generally conforms to those of the primitive mantle. The glimmerite and carbonate glimmerite exhibit enrichment in LILE, REE and HFSE. The Hf and Zr concentrations of the carbonate glimmerite are nevertheless as low as in the PM. The fenites are all enriched in elements presented in the spidergram, except for Ti, Y, Yb,V and Sc, which are only slightly depleted or enriched (Fig. 10d). The enrichment in REE of fenites is less important than in apatite, whereas their enrichments in Pb and HFSE strongly contrast with the signature of apatite (LA-ICPMS measurements). The Post Archean Australian Shale (PAAS)-normalized spidergrams are overall comparable to the PM-normalized ones (Fig. 10e and f). However, most of the elements are depleted compared to PAAS, except for Sr, LREE, P and Sc that are enriched in all rock types. Another notable discrepancy is the more pronounced depletion in LILE of the fenites.
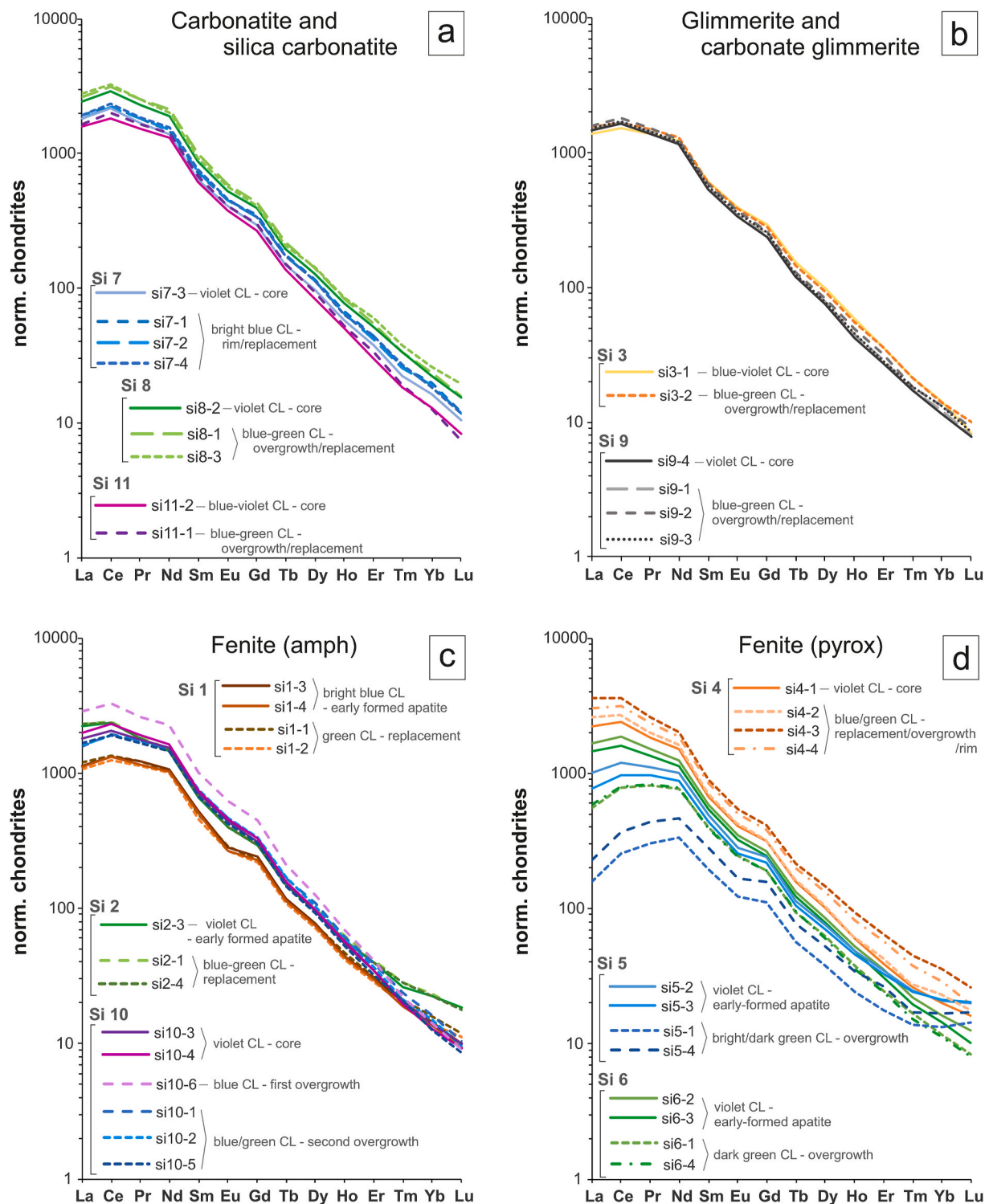
Cathodoluminescence spectra

Raman spectra converted to wavelength

Fig. 7. Representative spectra of apatite from various rocks of the Siilinjärvi Complex using cathodoluminescence (a,b,c) and Raman spectroscopy (d,e,f). (a) and (d) Spectra of apatite from carbonatite and silica carbonatite (samples Si11 and Si7); (b) and (e) Spectra of apatite from pyroxene-rich fenite (samples Si5 and Si6); (c) and (f) Spectra of apatite from amphibole-rich fenite (sample Si10).

Fig. 8. REE patterns of apatite in the different rock types of the Siilinjärvi Complex; (a) carbonatite and silica carbonatite, (b) glimmerite and carbonate glimmerite, (c) amphibole-rich fenite and (d) pyroxene-rich fenite; REE patterns are normalized to chondrite values from McDonough and Sun (1995).

5. Discussion

5.1. Apatite forming processes at Siilinjärvi and related REE content and distribution

5.1.1. Glimmerite and carbonatite series

The magmatic origin of apatite in the glimmerite-carbonatite series is confirmed by the blue cathodoluminescence of this mineral (e.g.,

Broom-Fendley et al., 2016; Decrée et al., 2016, 2020; Waychunas, 2002), the enrichment in LREE and the lack of complex textures such as turbid or conversion textures under CL (e.g., Broom-Fendley et al., 2017; Zirner et al., 2015). LIBS images of the investigated apatite ore (an apatite-rich carbonatite exploited for its very high P content; Fig. 3) show that apatite crystals could be associated with a distinct carbonatitic intrusion enriched in Na–K. This leads to the following inferences: (i) there were probably multiple pulses of carbonatite magma
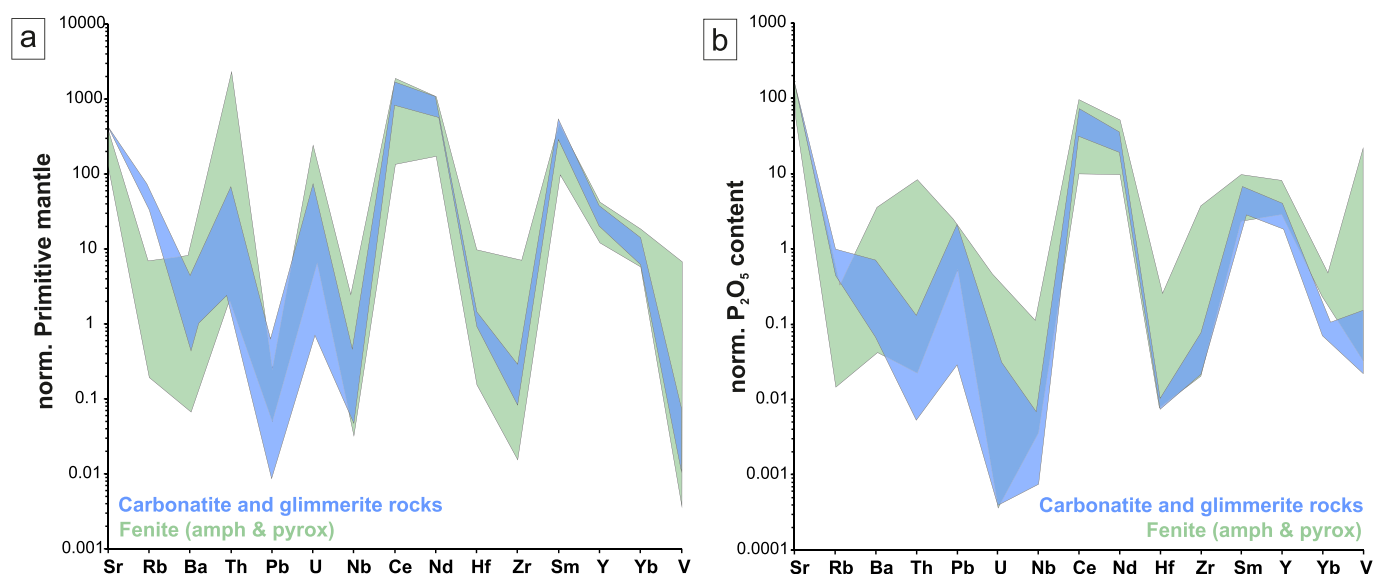
Fig. 9. Spidergrams generated from LA-ICPMS analyses and normalized to (a) the Primitive mantle (McDonough and Sun, 1995) and (b) to the P_2O_5 content (in wt. %, electron microprobe analyses).

intrusion at Siilinjärvi, as already suspected by Tichomirowa et al. (2006), with significant differences in magma chemistry; (ii) apatite was preferentially associated with discrete intrusions of Na- and K-rich carbonatite melts. Such enrichment could relate to the fenitization processes and the circulation of Na–K-rich fluids during mid-crustal pre-emplacement evolution of the carbonatite, as suggested by Poutiainen (1995) based on the microthermometric study of apatite.

A major evolution trend regarding the distribution of REE in apatite is revealed by CL imaging and LA-ICPMS analyses. An overall increase in REE content – concomitant with an increase in Sr and Y (Fig. 9a and b) – is observed during apatite deposition in glimmerite and carbonatite. Early-formed violet-luminescent apatite was replaced by a blue-green-luminescent apatite that is more strongly activated by Nd and enriched in REE compared to the former (Figs. 3 and 8a and b). Similarly, the blue-luminescent outer part of apatite crystals (rims or overgrowths) has a CL that is more strongly activated by Nd than in early apatite (Figs. 3 and 8a and b). An increase in REE uptake from early-formed to later-formed apatite can be reached by two processes:

(i) The fractionation of a large amount of co-precipitating minerals – here calcite and phlogopite - could theoretically influence the REE budget of the residual melt (e.g., Bühn et al., 2001; Chakhmouradian et al., 2017). However, this possibility can be largely discarded in our case for the following reasons. First, the removal of REE hosted by phlogopite should not significantly affect the REE distribution and content in later formed apatite because the REE content of this mineral is very low, that is, hardly above the detection limits (Chakhmouradian et al., 2017). Moreover, an increase of the $(La/Yb)_N$ ratio of the residual melt is expected after crystallization of a large quantity of calcite (Bühn et al., 2001). Such a trend is not observed in the late generations of apatite, which supposedly crystallized in equilibrium with the residual melt.

(ii) Alternatively, the REE enrichment during apatite deposition could be due to a more evolved magmatic/metasomatic input. Such an input could come via the intrusion of a fresh magma enriched in REE (as the one observed on the LIBS images). This intrusion would lead to the re-equilibration of earlier-formed apatite with the intruding magma, likely through sub-solidus diffusion at the magmatic stage (e.g., Harlov et al., 2005; Chakhmouradian et al., 2017). This was already suggested for zircon close to warm and thick calcite veins at Siilinjärvi

(Tichomirowa et al., 2013). Moreover, Tichomirowa et al. (2006) noticed a change of apatite CL color from purple to blue in contact with the latest generation of carbonatite. We have shown here that this change in color is associated with an increase in REE. All these arguments suggest that a late carbonatite pulse associated with the development of alkali-rich fluids that caused widespread fenitization could be responsible for a significant input of P and REE into the system, affecting all the previously emplaced rocks of the glimmerite-carbonatite series. This is consistent with the fact that REE are typically found in more evolved magmas (e.g., Mariano, 1989; Elliott et al., 2018; Simandl and Paradis, 2018).

5.1.2. Fenite

In amphibole- and pyroxene-rich fenites, apatite displays a complex zonation (alteration and conversion textures), which can be regarded as the product of apatite re-equilibration with highly evolved melts and/or fluids (e.g., Zirner et al., 2015; Broom-Fendley et al., 2017; Chakhmouradian et al., 2017; Decrée et al., 2020). Late-stage interactions with water-rich fluids were already assumed at Siilinjärvi, based on the general tendency of decreasing Sr concentrations with increasing $\delta^{18}O$ ratios (Tichomirowa et al., 2006). The REE content and distribution follow two major evolution trends in the investigated apatite within fenite:

(i) Apatite grains can exhibit an increasing Nd activation under CL towards their outer rim, as overgrowths after resorption, and in the inner part of the grains, while replacing early-formed violet-luminescent apatite. Both overgrowth and replacement zones show a blue-green luminescence and an increase in REE content (samples Si2 and Si4; Fig. 5a and b and Fig. 8c and d).

(ii) The second trend is characterized by a strong decrease in Nd-activation in green-luminescent rims and overgrowths (in samples Si5 and Si6; Fig. 5e–g). This decrease in REE is coupled with a substantial LREE loss (and a stronger Eu negative anomaly) that modifies the shape of the REE patterns (Fig. 8d) and a loss in other elements, such as Sr and Y (Fig. 11a and b). It is worth mentioning that several apatite grains record both trends, with a first phase of growth/replacement characterized by a REE-enrichment and a second phase of growth recording a slight depletion in REE (samples Si1 and Si10; Fig. 5c and d and Fig. 8c).

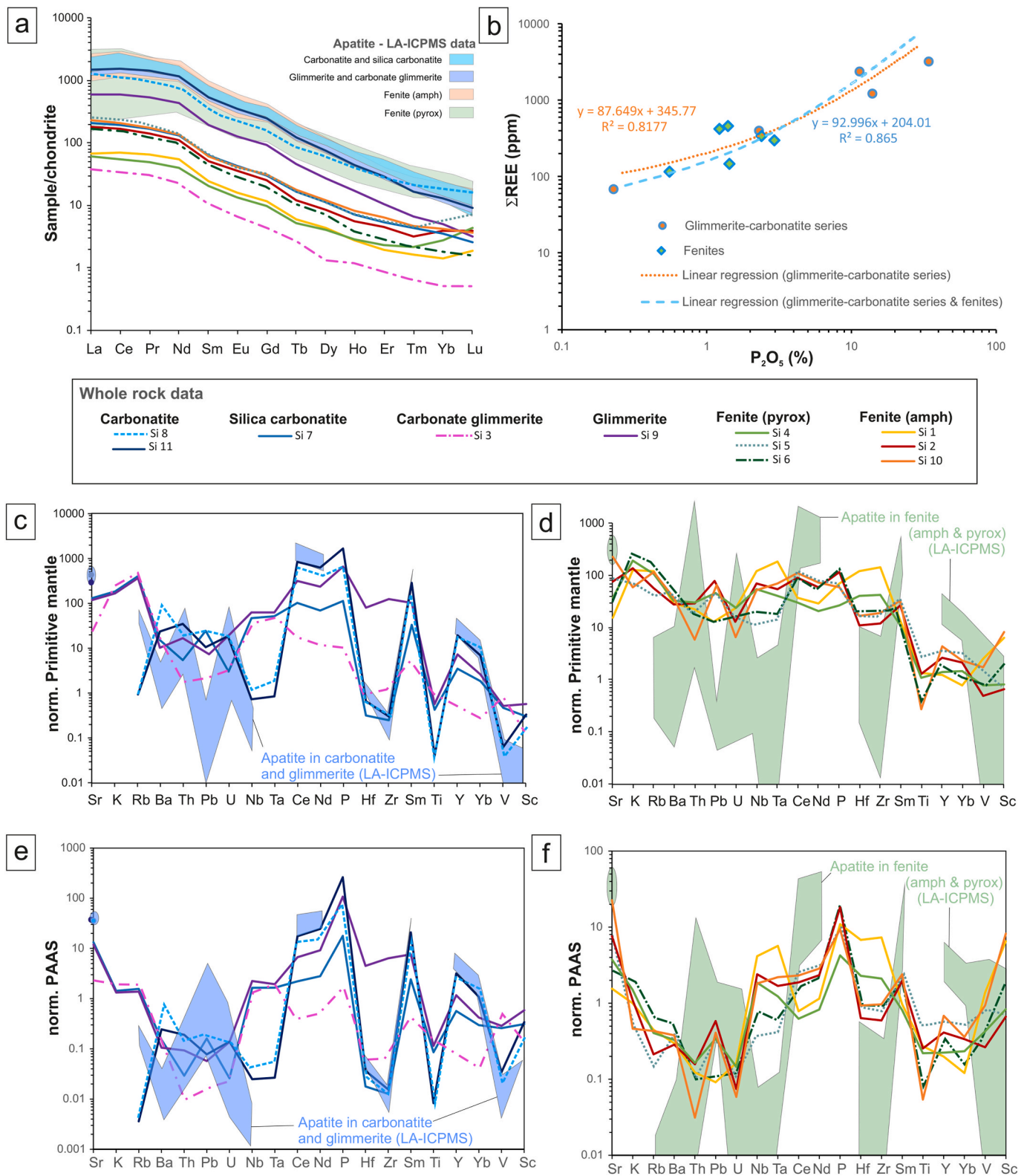Considering the above contrasting trends, at least two types of melt/

Fig. 10. (a) REE patterns for whole rock data of the Siilinjärvi rocks. REE patterns of apatite (LA-ICPMS data) are given for comparison. Data are normalized to chondrites (McDonough and Sun, 1995), (b) correlation for whole rock analyses between total REE content and P_2O_5 content, (c–f) spidergrams of the Siilinjärvi rocks comparing whole rock analyses and LA-ICPMS analyses of apatite. Normalization to the Primitive mantle (McDonough and Sun, 1995) (c–d) and to the Post Archean Australian Shales (PAAS; Condie, 1993) (e–f).
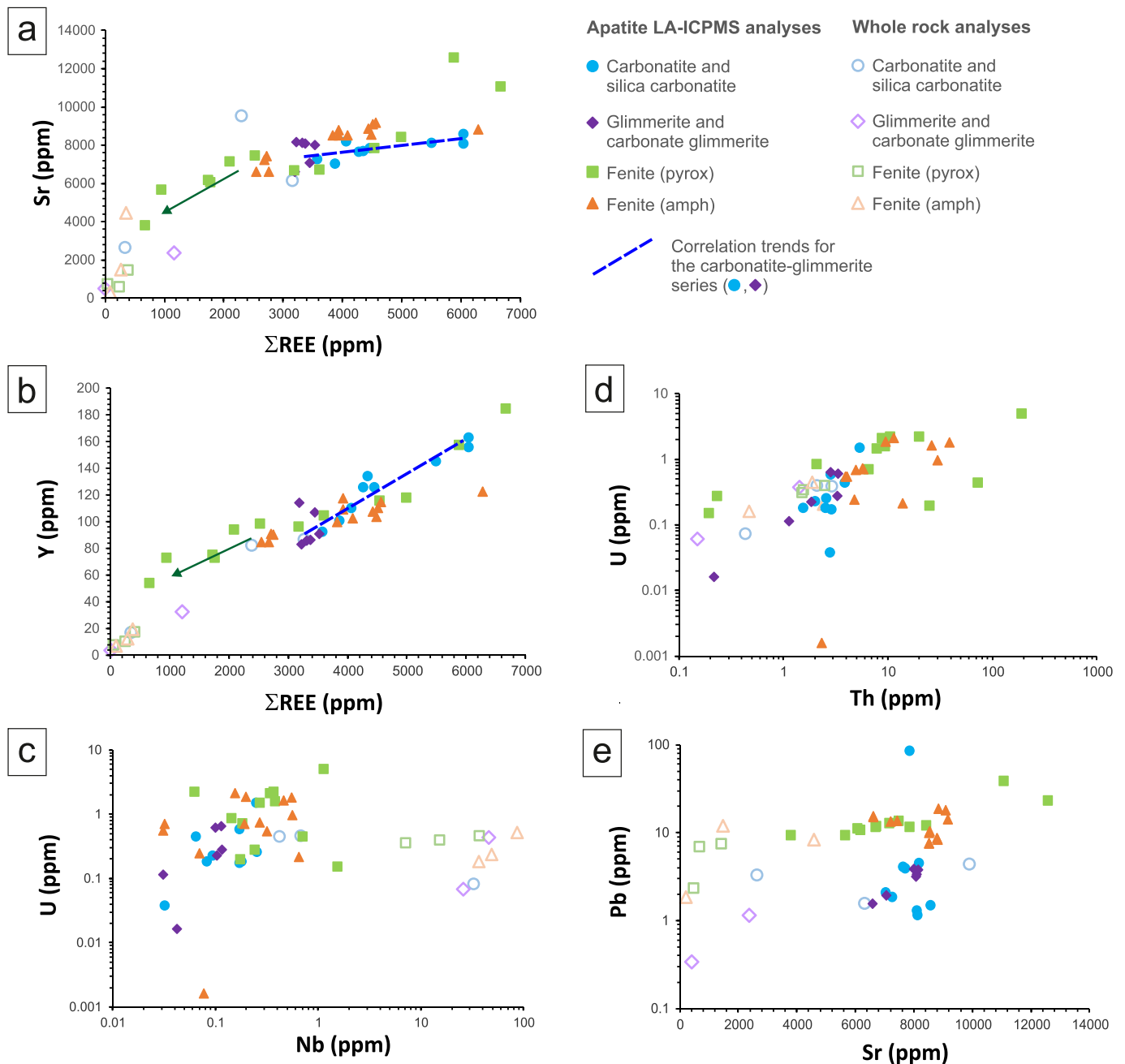
Fig. 11. Correlations for LA-ICPMS analyses between Sr and total REE content (a), Y and total REE content (b), U and Nb (c), U and Th (d) and Pb and Sr (e). Whole rock data are given for comparison.

fluid-rock interactions could explain the observed phenomena. The REE enrichment could involve Na–K-rich fluids during early (pre-emplacement) evolution of the carbonatite. These fluids are likely enriched in P and REE, as already evoked in section 5.1.1. Interacting with them, the early formed apatite would have been enriched in REE through coupled dissolution–reprecipitation processes (e.g., Zirner et al., 2015). Other elements – namely, Nb, Th, Pb (and U to some extent) – could be concentrated when interacting with these fluids. Their contents in apatite hosted by fenite are higher than those in apatite from the carbonatite-glimmerite series (Fig. 11c–e).

Conversely, the decrease in LREE in apatite is commonly attributed to the mobilization of these elements during fluid flow through the rock (e.g., Harlov et al., 2002). The LREE are more easily mobilized than M/HREE during fluid-rock interactions and show greater stability as chloride or fluoride complexes (e.g., Broom-Fendley et al., 2016; Elliott

et al., 2018; Krneta et al., 2018). The more pronounced negative Eu anomalies (0.73 < Eu/Eu*<0.83) are likely due to the extraction of divalent Eu via a high-temperature aqueous fluid evolving from the magma (Bühn et al., 2001). The assemblage of green-luminescent apatite (which is less enriched in REE) and REE mineral phases as britholite and monazite at the apatite rim would have formed at the expense of the REE-rich apatite through coupled substitution and mass transfer (e.g., Zirner et al., 2015; Giebel et al., 2017).

5.1.3. Prospect of REE quantitation in apatite using CL and Raman spectroscopy

Fluorescence and CL activation can be deduced from the observation of the cathodoluminescence and Raman spectra. At a first glance, it appears that the relative intensity of the emission peak of a specific luminescence activator can be correlated with its concentration. For

instance, in carbonatite, the overall luminescence is more intense in the REE-rich green-luminescent apatite of the replacement zones than in the early-formed violet luminescing apatite, which is less enriched in REE (Fig. 7a,d). An attempt was made to correlate the luminescence spectra and the REE content of apatite more accurately. Neodymium appeared as a good candidate for such a purpose, because the emission multiplet of Nd^{3+} in the near-infrared is free from any interference with other REE and the background signal is low. After subtraction of the background, the area under the peaks was measured between ~850 and ~950 nm. The good correlation between the Nd content as measured using LA-ICPMS and spectroscopic measurements for both fluorescence and cathodoluminescence spectra is presented in Fig. 12. It shows that the spectral signal of apatite using CL and Raman can be used to estimate the relative content of Nd. These correlations could be undoubtedly improved with more careful acquisition settings, data processing (especially background subtraction) and a more rigorous chemometric approach. An absolute concentration could be obtained if a minimum of geochemical data is provided for calibration. Of course, this method should be extended to more types of apatite from other carbonatites and other environments to validate the observed correlation. Nevertheless, the currently available data confirm that spectroscopic analysis of luminescence is a helpful tool to assess the REE potential of apatite with relatively little effort.

5.2. Reassessment of the economic potential regarding strategic elements

The estimation of the ore reserves at Siilinjärvi as per January 2014 was 234 Mt at an average grade of 4 wt% P_2O_5. Almost all the rocks of the glimmerite-carbonatite series can be considered economic for apatite exploitation (O'Brien et al., 2015). The analyses performed in the frame of this study confirm the enrichment in phosphate of these rocks ($2.32 < P_2O_5 < 34.18$ wt%), apart from the carbonate glimmerite that contains only 0.23 wt% P_2O_5. In the Siilinjärvi mine, fenites are

stockpiled separately (O'Brien et al., 2015), though some of these rocks show a promising phosphate content (two samples at 2.4 and 2.9 wt% P_2O_5), close to the average grade of the rocks that are currently mined.

Beside phosphate, numerous commodities can be recovered from deposits associated with carbonatites and related alkaline complexes, such as Nb, Zr, Hf and REE (e.g., Pell, 1996). The spidergrams in Fig. 10 show that none of these elements are concentrated at Siilinjärvi, apart from the REE. Whether it is in the rocks pertaining to the glimmerite-carbonatite series or in fenites, the REE content of the rocks correlates well with their P_2O_5 concentration (Fig. 10b). These correlations can be used to roughly estimate the REE reserves at Siilinjärvi. Based on the latter and on an average content of 4 wt% P_2O_5 in the rocks exploited (O'Brien et al., 2015), two average hypothetical REE contents were calculated, depending on the correlation used: (i) 576 ppm, using the equation based on all rock types (Fig. 10b), and (ii) 697 ppm using the equation considering only the rocks currently mined as phosphate (i. e. the glimmerite-carbonatite series; Fig. 10b). As a reserve of roughly 200 Mt remains to be exploited, the REE reserve should approximate ~133,000 t of Total Rare Earth Oxide (TREO) (using an average grade of 576 ppm) or ~161,000 t of TREO (using an average grade of 697 ppm) in the phosphate deposit. A large part of the REE must be present in apatite that contains up to 0.66 wt% REE, even though other REE-minerals are also present as scattered minute grains in the different rocks (as observed on the LIBS images, Figs. 3, 5h and 6). The exploitation of REE as a by-product of the apatite could be interesting at Siilinjärvi, and probably in other alkaline complexes as well. In the Khibina alkaline massif (Kola Peninsula, Russia), an increase in production of REE would be achieved by extracting the REE from apatite through a hydrochloric acid treatment (with recovery rates of ~80% REE; Pereira and Bilal, 2012). Considering the relative ease of REE extraction from apatite (e.g. Emsbo et al., 2015), the potential reserves of REE at Siilinjärvi (133,000–161,000 tons of REE_2O_3) and assuming that a large part of REE is locked into the structure of apatite, the beneficiation of REE as a by-product of the Siilinjärvi phosphates could be of economic interest.

6. Summary and conclusions

Apatite from the Neoarchean carbonatite complex of Siilinjärvi has been investigated for its chemistry and optical spectroscopy (CL, Raman spectroscopy, LIBS). The aim was to decipher the processes leading to the formation of apatite and controlling the distribution of REE in this mineral. In the glimmerite-carbonatite series, the blue-violet CL and LREE enrichment corroborate a previously assumed igneous origin of the apatite. The REE enrichment in alteration zones and at the rim of apatite crystals reveals re-equilibration of early formed apatite with a REE-rich fresh carbonatite magma. This magma, which is one of the last intruded, caused a significant input of P and REE into the system. The late carbonatite also recorded interactions with alkali-rich fluids, likely in connection with fenitization. In fenite, alteration textures emphasize fluid-rock/magma interactions at various stages of apatite crystallization. A first event led to enrichment in REE of the early formed apatite. This enrichment was likely due to interaction with REE-rich fluids related to fenitization. Local depletion of apatite in LREE is ascribed to a late-magmatic or hydrothermal stage.

Spectroscopic methods used here constitute powerful and inexpensive tools for exploration. In addition to bringing crucial information about mineralization events, LIBS mapping makes it possible to map elemental distribution (and speciation) of P and REE in the rocks. Raman and CL spectroscopy give clues regarding enrichment in REE of apatite, as illustrated by (i) the spectral CL of the Nd^{3+} emission at 880 nm that quickly reveals the REE distribution and enrichment in apatite, and (ii) fluorescence (photoluminescence) and cathodoluminescence spectra that enable fast qualitative assessments of the REE enrichment in apatite based on the observed correlation between spectroscopic and geochemical data, with some insight into (semi)-quantification.
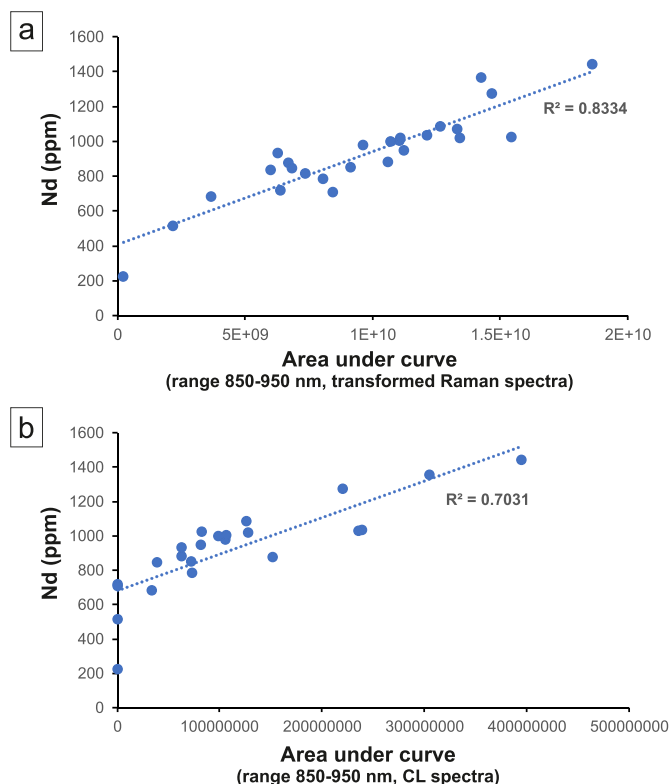

Fig. 12. Correlation between Nd content and area under curve between 850 and 950 nm for (a) transformed Raman spectra (Raman shift converted into wavelength) and (b) CL spectra.

Finally, the geochemical data obtained on whole rock samples show that part of the fenites could be considered for exploitation, because their phosphate content is close to the average content of the rocks currently mined. In addition, the REE and phosphate contents correlate well in all of the investigated rocks. A rough estimate based on this correlation and the available data on reserves suggests that REE could constitute an economically interesting by-product of the Siilinjärvi phosphates.

Declaration of competing interest

The authors declare that they have no known competing financial interests or personal relationships that could have appeared to influence the work reported in this paper.

Appendix A. Supplementary data

Supplementary data to this article can be found online at https://doi.org/10.1016/j.apgeochem.2020.104778.

References

Al Ani, T., 2013. Mineralogy and petrography of Siilinjärvi carbonatite and glimmerite rocks, eastern Finland. Geol. Survey. Fin. Report 164p. https://tupa.gtk.fi/raportti/arkisto/164_2013.pdf.

Alvarez Llamas, C., Pisonero, J., Bordel, N., 2017. Novel approach for quantitative LIBS fluorine analysis using CaF emission in calcium-free samples. J. Anal. Atom. Spectr. 32 (1), 162–166.

Baele, J.M., Decrée, S., Rusk, B., 2019. Cathodoluminescence applied to ore geology and exploration. In: Decrée, S., Robb, L. (Eds.), Ore Deposits: Origin, Exploration, and Exploitation. Wiley, New York, pp. 131–161.

Bayanova, T.B., 2006. Baddeleyite: a promising geochronometer for alkaline and basic magmatism. Petrol 14, 187–200.

Blanc, P., Baumer, A., Cesbron, F., Ohnenstetter, D., Panczer, G., Rémond, G., 2000. Systematic cathodoluminescence spectral analysis of synthetic doped minerals: anhydrite, apatite, calcite, fluorite, scheelite and zircon. In: Pagel, M., et al. (Eds.), Cathodoluminescence in Geosciences. Springer Verlag, Heidelberg New-York, pp. 127–160.

Broom-Fendley, S., Heaton, T., Wall, F., Gunn, G., 2016. Tracing the fluid source of heavy REE mineralisation in carbonatites using a novel method of oxygen-isotope analysis in apatite: the example of Songwe Hill. Malawi. Chem. Geol. 440, 275–287.

Broom-Fendley, S., Brady, A.E., Wall, F., Gunn, G., Dawes, W., 2017. REE minerals at the Songwe Hill carbonatite, Malawi: HREE-enrichment in late-stage apatite. Ore Geol. Rev. 81, 23–41.

Bühn, B., Dörr, W., Brauns, C.M., 2001. Petrology and age of the Otjisazu carbonatite complex, Namibia: implications for the pre-and synorogenic Damaran evolution. J. Afr. Earth Sci. 32, 1–17.

Chakhmouradian, A.R., Reguir, E.P., Zaitsev, A.N., et al., 2017. Apatite in carbonatitic rocks: compositional variation, zoning, element partitioning and petrogenetic significance. Lithos 274, 188–213.

Condie, K.C., 1993. Chemical composition and evolution of the upper continental crust: contrasting results from surface samples and shales. Chem. Geol. 104, 1–37. https://doi.org/10.1016/0009-2541(93)90140-E.

Decrée, S., Boulvais, P., Cobert, C., et al., 2015. Structurally-controlled hydrothermal alteration in the upper ruvubu alkaline plutonic complex (Burundi): implications for REE and HFSE mobilities. Precambr. Res. 269, 281–295.

Decrée, S., Boulvais, P., Tack, L., André, L., Baele, J.M., 2016. Fluorapatite in carbonatite-related phosphate deposits: the case of the Matongo carbonatite (Burundi). Miner. Dep. 51, 453–466.

Decrée, S., Ihlen, P.M., Schiellerup, H., Hallberg, A., Demetriades, A., Raha, M., Soesoo, A., 2017. Potential of phosphate deposits in Europe. SGA News 41, 14–20. https://e-sga.org/fileadmin/sga/newsletter/news41/SGANews41.pdf.

Decrée, S., Cawthorn, G., Deloule, E., et al., 2020. Unravelling the processes controlling apatite formation in the Phalaborwa Complex (South Africa) based on combined cathodoluminescence, LA-ICPMS and in-situ O and Sr isotope analyses. Contrib. Mineral. Petrol. 175, 34. https://doi.org/10.1007/s00410-020-1671-6.

Demény, A., Sitnikova, M.A., Karchevsky, P.I., 2004. Stable C and O isotope compositions of carbonatite complexes of the Kola Alkaline Province: phoscorite-carbonatite relationships and source compositions. In: Wall, F., Zaitsev, A. (Eds.), Phoscorites and Carbonatites from Mantle to Mine: the Key Example of the Kola Alkaline Province. Mineralogical Society Series 10, pp. 407–431.

Elliott, H.A.L., Wall, F., Chakhmouradian, A.R., et al., 2018. Fenites associated with carbonatite complexes: a review. Ore Geol. Rev. 93, 38–59.

Emsbo, P., McLaughlin, P.I., Breit, G.N., du Bray, E.A., Koenig, A.E., 2015. Rare earth elements in sedimentary phosphate deposits: solution to the global REE crisis? Gondwana Res. 27, 776–785.

EC (European Commission), 2014. On the review of the list of critical raw materials for the EU and the implementation of the Raw Materials Initiative. http://eur-lex.europa.eu/legal-content/EN/TXT/PDF/?uri=CELEX:52014DC0297&from=EN. (Accessed 9 December 2016).

Giebel, R.J., Gauert, C.D., Marks, M.A., Costin, G., Markl, G., 2017. Multi-stage formation of REE minerals in the palabora carbonatite complex, South Africa. Am. Miner. 102, 1218–1233.

Goldoff, B., Webster, J.D., Harlov, D.E., 2012. Characterization of fluor-chlorapatites by electron probe microanalysis with a focus on time-dependent intensity variation of halogens. Am. Miner. 97, 1103–1115.

Goodenough, K.M., Schilling, J., Jonsson, E., et al., 2016. Europe's rare earth element resource potential: an overview of REE metallogenetic provinces and their geodynamic setting. Ore Geol. Rev. 72, 838–856.

Harlov, D.E., Andersson, U.B., Förster, H.J., Nyström, J.O., Dulski, P., Broman, C., 2002. Apatite-monazite relations in the Kiirunavaara magnetite-apatite ore, northern Sweden. Chem. Geol. 191, 47–72.

Harlov, D.E., Wirth, R., Förster, H.J., 2005. An experimental study of dissolution–reprecipitation in fluorapatite: fluid infiltration and the formation of monazite. Contrib. Miner. Petrol. 150, 268–286.

Harmon, R.S., Lawley, C.J., Watts, J., Harraden, C.L., Somers, A.M., Hark, R.R., 2019. Laser-induced breakdown spectroscopy—an emerging analytical tool for mineral exploration. Minerals 9, 718.

Hornig-Kjarsgaard, I., 1998. Rare earth elements in sövitic carbonatites and their mineral phases. J. Petrol. 39, 2105–2121.

Hoshino, M., Sanematsu, K., Watanabe, Y., 2016. REE mineralogy and resources. In: Bünzli, J.C., et al. (Eds.), Handbook on the Physics and Chemistry of Rare Earths, vol. 49. Elsevier, pp. 129–291.

Hughes, J.M., Cameron, M., Mariano, A.N., 1991. Rare-earth-element ordering and structural variations in natural rare-earth-bearing apatites. Am. Miner. 76, 1165–1173.

Ihlen, P.M., Schiellerup, H., Gautneb, H., Skår, Ø., 2014. Characterization of apatite resources in Norway and their REE potential—a review. Ore Geol. Rev. 58, 126–147.

Jochum, K.P., Weis, U., Stoll, B., et al., 2011. Determination of reference values for NIST SRM 610–617 glasses following ISO guidelines. Geostand. Geoanal. Res. 35, 397–429.

Kempe, U., Götze, J., 2002. Cathodoluminecence (CL) behaviour and crystal chemistry of apatite from rare-metal deposits. Min. Mag. 66, 151–172.

Krneta, S., Ciobanu, C., Cook, N., Ehrig, K., 2018. Numerical modeling of REE fractionation patterns in fluorapatite from the olympic dam deposit (South Australia). Minerals 8, 342.

Longerich, H.P., Jackson, S.E., Günther, D., 1996. Inter-laboratory note. Laser ablation inductively coupled plasma mass spectrometric transient signal data acquisition and analyte concentration calculation. J. Anal. At. Spectrom. 11, 899–904.

Mariano, A.N., 1989. Nature of economic mineralization in carbonatites and related rocks. In: Bell, K. (Ed.), Carbonatites: Genesis and Evolution. Unwin Hyman, pp. 149–176.

Marshall, D.J., 1988. Cathodoluminescence of Geological Materials. Hyman, Boston, p. 146.

McDonough, W.F., Sun, S.S., 1995. The composition of the Earth. Chem. Geol. 120, 223–253.

Mitchell, R.H., 2014. Cathodoluminescence of Apatite. Mineralogical Association of Canada Short Course 45. Fredericton NB, pp. 143–167. May 2014.

Mitchell, R.H., Xiong, J., Mariano, A.N., Fleet, M.E., 1997. Rare-earth-element-activated cathodoluminescence in apatite. Can. Mineral. 35, 979–998.

Mitchell, R.H., Wahl, R., Cohen, A., 2020. Mineralogy and genesis of pyrochlore apatitite from the Good Hope Carbonatite, Ontario: a potential niobium deposit. Mineral. Mag. 84, 81–91.

Nadeau, S.L., Epstein, S., Stolper, E., 1999. Hydrogen and carbon abundances and isotopic ratios in apatite from alkaline intrusive complexes, with a focus on carbonatites. Geochim. Cosmochim. Acta 63, 1837–1851.

Niiranen, T., Lahti, I., Nykänen, V., 2015. The orogenic gold potential of the Central Lapland greenstone belt, northern Fennoscandian Shield. In: Maier, W.D., Lahtinen, R., O'Brien, H. (Eds.), Mineral Deposits of Finland. Elsevier, pp. 733–752.

Notholt, A.J.G., Highley, D.E., Slansky, M., 1979. Raw Materials Research and Development IV. Dossier on Phosphate. Commission of the European Communities, Brussels, p. 234. http://aei.pitt.edu/51552/1/B0448.pdf.

O'Brien, H., Heilimo, E., Heino, P., 2015. The Archean Siilinjärvi carbonatite complex. In: Maier, W.D., Lahtinen, R., O'Brien, H. (Eds.), Mineral Deposits of Finland. Elsevier, pp. 327–343.

Pan, Y., Fleet, M.E., 2002. Compositions of the apatite-group minerals: substitution mechanisms and controlling factors. Rev. Miner. Geochem. 48, 13–49.

Paton, C., Hellstrom, J., Paul, B., et al., 2011. Iolite: freeware for the visualisation and processing of mass spectrometric data. J. Anal. At. Spectrom. 26, 2508–2518.

Pell, J., 1996. Mineral deposits associated with carbonatites and related alkaline igneous rocks. In: Mitchell, R.H. (Ed.), Undersaturated Alkaline Rocks: Mineralogy, Petrogenesis, and Economic Potential. Short Course Series 24. Mineralogical Association of Canada, Winnipeg, pp. 271–310.

Pereira, F., Bilal, E., 2012. Phosphoric acid extraction and rare earth recovery from apatites of the Brazilian phosphatic ores. Rom. J. Miner. Dep. 85, 49–52.

Potts, P.J., Tindle, A.G., 1989. Analytical characteristics of a multilayer dispersion element (2d=60Å) in the determination of fluorine in minerals by electron microprobe. Miner. Mag. 53, 357–362.

Poutiainen, M., 1995. Fluids in the Siilinjärvi carbonatite complex, eastern Finland: fluid inclusion evidence for the formation conditions of zircon and apatite. Bull. Geol. Soc. Fin. 67, 3–18.

Puustinen, K., 1969. The carbonatite of Siilinjairvi in the Precambrian of Eastern Finland - a preliminary report. Lithos 3, 89–92.

Puustinen, K., 1971. Geology of the Siilinjärvi carbonatite complex, eastern Finland. Bull. Comm. Geol. Fin. 249, 43p. http://tupa.gtk.fi/julkaisu/bulletin/bt_249.pdf.

Puustinen, K., Kauppinen, H., 1989. The siilinjäri carbonatite complex, eastern Finland. In: Notholt, A.J.G., Sheldon, R.P., Davidson, D. (Eds.), Phosphate Deposits of the World: Volume 2, Phosphate Rock Resources. Cambridge University Press, pp. 394–397.

Roeder, P.L., MacArthur, D., Ma, X.P., Palmer, G.R., Mariano, A.N., 1987. Cathodoluminescence and microprobe study of rare-earth elements in apatite. Am. Miner. 72, 801–811.

Rueden, C.T., Schindelin, J., Hiner, M.C., et al., 2017. ImageJ2: ImageJ for the next generation of scientific image data. BMC Bioinf. 18 (1), 529. https://doi.org/10.1186/s12859-017-1934-z. PMID 29187165. https://bmcbioinformatics.biomedcentral.com/track/pdf/10.1186/s12859-017-1934-z.

Simandl, G.J., Paradis, S., 2018. Carbonatites: related ore deposits, resources, footprint, and exploration methods. Applied Earth Sci 127, 123–152.

Stormer, J.C., Pierson, M.L., Tacker, R.C., 1993. Variation of F and Cl X-ray intensity due to anisotropic diffusion in apatite during electron microprobe analysis. Am. Miner. 78, 641–648.

Tichomirowa, M., Grosche, G., Götze, J., et al., 2006. The mineral isotope composition of two Precambrian carbonatite complexes from the Kola Alkaline Province–Alteration versus primary magmatic signatures. Lithos 91, 229–249.

Tichomirowa, M., Whitehouse, M.J., Gerdes, A., Götze, J., Schulz, B., Belyatsky, B.V., 2013. Different zircon recrystallization types in carbonatites caused by magma mixing: evidence from U–Pb dating, trace element and isotope composition (Hf and O) of zircons from two Precambrian carbonatites from Fennoscandia. Chem. Geol. 353, 173–198.

Van Straaten, H.P., 2002. Rocks for Crops. Agrominerals of Sub-saharan Africa. International centre for research in agroforestry, Nairobi, Kenya, p. 338. http://apps.worldagroforestry.org/Units/Library/Books/PDFs/11_Rocks_for_crops.pdf.

Verwoed, W.J., 1986. Mineral deposits associated with carbonatites and alkaline rocks. In: Anhaeusser, C., Maske, S. (Eds.), Mineral Deposits of Southern Africa. Geol. Soc. S. Afr., pp. 2173–2191

Walter, A.V., Nahon, D., Flicoteaux, R., Girard, J.P., Melfi, A., 1995. Behaviour of major and trace elements and fractionation of REE under tropical weathering of a typical apatite-rich carbonatite from Brazil. Earth Planet Sci. Lett. 136, 591–602.

Waychunas, G.A., 2002. Apatite luminescence. In: Kohn, M.J., Rakovan, J., Hughes, J.M. (Eds.), Reviews in Mineralogy and Geochemistry Volume 48 – Phosphates. Mineralogical Society of America, Washington DC, pp. 701–742.

Zirner, A.L., Marks, M.A., Wenzel, T., Jacob, D.E., Markl, G., 2015. Rare earth elements in apatite as a monitor of magmatic and metasomatic processes: the Ilímaussaq complex, South Greenland. Lithos 228, 12–22.

Zozulya, D.R., Bayanova, T.B., Serov, P.N., 2007. Age and isotopic geochemical characteristics of Archean carbonatites and alkaline rocks of the Baltic Shield. Doklady Earth Sci 415, 874–879.